BRNO UNIVERSITY OF TECHNOLOGY
VYSOKÉ UČENÍ TECHNICKÉ V BRNĚ

FACULTY OF ELECTRICAL ENGINEERING AND COMMUNICATION
ÚSTAV RADIOELEKTRONIKY

FAKULTA ELEKTROTECHNIKY A KOMUNIKAČNÍCH TECHNOLOGIÍ
DEPARTMENT OF RADIOELECTRONICS

PARAMETERS OF COMMUNICATION SYSTEMS BASED ON OFDM-CDMA

DOCTORAL THESIS
DIZERTAČNI PRÁCE

AUTHOR
AUTOR PRÁCE

Ing. JIŘÍ BLUMENSTEIN

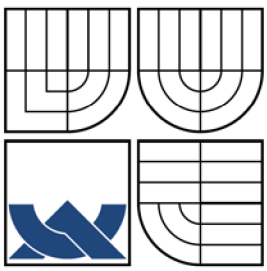

BRNO UNIVERSITY OF TECHNOLOGY
VYSOKÉ UČENÍ TECHNICKÉ V BRNĚ

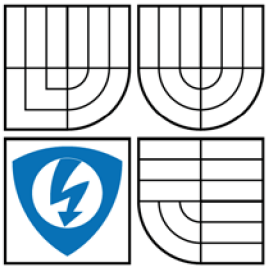

FACULTY OF ELECTRICAL ENGINEERING AND COMMUNICATION
ÚSTAV RADIOELEKTRONIKY

FAKULTA ELEKTROTECHNIKY A KOMUNIKAČNÍCH TECHNOLOGIÍ
DEPARTMENT OF RADIOELECTRONICS

PARAMETERS OF COMMUNICATION SYSTEMS BASED ON OFDM-CDMA

PARAMETRY KOMUNIKAČNÍCH SYSTÉMŮ ZALOŽENÝCH NA OFDM-CDMA

DOCTORAL THESIS
DIZERTAČNI PRÁCE

AUTHOR
AUTOR PRÁCE
Ing. JIŘÍ BLUMENSTEIN

SUPERVISOR
VEDOUCÍ PRÁCE
Ing. ZBYNĚK FEDRA, Ph.D.

BRNO 2012

BLUMENSTEIN, J. *Parameters of communication systems based on OFDM-CDMA*. Brno: Vysoké učení technické v Brně, Fakulta elektrotechniky a komunikačních technologií, 2011. 76 s.

Abstract

The focus of this research is in the area of modeling and evaluating of the wireless systems with two dimensional signal spreading, it's key parameters and dependencies on other features in modern wireless communication chain.

The research method adopted in this dissertation includes a development of Matlab based simulators which exploits a statistical approach to show a contribution of proposed algorithms. Furthermore, a model of physical layer of the 3rd Generation Partnership Project Long Term Evolution (3GPP LTE), developed by the Vienna University of Technology, was utilized as a simulation environment suitable for implementation of a two dimensional (2D) signal spreading method and its evaluation as well as comparison of achieved results with the state-of-the-art systems.

The findings from this research provide evidence that the Variable Spreading Factor - Orthogonal Code Frequency Division Multiplex (hereafter VSF-OFCDM) employing a 2D spreading is a promising wireless access scheme superior to Orthogonal Division Frequency Multiplex (OFDM) or Code Division Multiple Access (CDMA) and is capable to significantly increase the data rates in wireless transmission due to the capability of such system to effectively cope with fast time and frequency fluctuations in the wireless transmission channel.

Keywords

VSF-OFCDMA, LTE, 2D spreading, PAPR, Power amplifier, USRP

Abstrakt

Cíl disertační práce leží v oblasti modelování a vyhodnocení bezdrátových komunikačních systémů s dvojrozměrným rozprostíráním signálu a jejich klíčových parametrů v závislosti na vybraných vlastnostech moderního bezdrátového komunikačního řetězce.

Výzkumné metody použité v této práci spočívají především ve vývoji softwarového simulátoru pro prostředí Matlab, s jehož pomocí, a s využitím statistického přístupu, jsou navržené algoritmy ověřeny. Dále je použit simulátor fyzické vrstvy dle 3rd Generation Partnership Project Long Term Evolution (3GPP LTE), vyvinutý na Technické univerzitě ve Vídni. Tento představuje ideální platformu pro implementaci metody dvojrozměrného (2D) rozprostírání a její vyhodnocení s přihlédnutím k současným bezdrátovým komunikačním systémům.

Zjištění prezentovaná v této práci představují především ověření účinnosti systému nazvaného jako Variable Spreading Factor - Orthogonal Code Frequency Division Multiplex (VSF-OFCDM), který využívá principu 2D rozprostírání signálu a zjištění, že VSF-OFCDM systém překonává systémy využívající Orthogonal Division Frequency Multiplex (OFDM), nebo Code Division Multiple Access (CDMA). Dále byla navržena metoda 2D rozprostírání signálu v systému LTE, kde se též potvrdila její účinnost. Díky účinnějšímu potlačení vlivu rychlé variace přenosového kanálu v závislosti na frekvenci a čase, dosahuje systém VSF-OFCDM znatelně vyšší datové prostupnosti.

Klíčová slova

VSF-OFCDMA, LTE, 2D rozprostírání, PAPR, Výkonový zesilovač, USRP

Declaration

I declare that I have elaborated my doctoral thesis on the theme of "Parametry komunikačních systémů založených na OFDM-CDMA" independently, under the supervision of the doctoral thesis supervisor and with the use of technical literature and other sources of information which are all quoted in the thesis and detailed in the list of literature at the end of the thesis. As the author of the doctoral thesis I furthermore declare that, concerning the creation of this doctoral thesis, I have not infringed any copyright. In particular, I have not unlawfully encroached on anyone's personal copyright and I am fully aware of the consequences in the case of breaking Regulation S 11 and the following of the Copyright Act No 121/2000 Vol., including the possible consequences of criminal law resulted from Regulation S 152 of Criminal Act No 140/1961 Vol.

Brno

(author's signature)

I would like to thank my supervisor Ing. Zbyňek Fedra, Ph.D. for his comprehensive support and help during my studies. I am also grateful to the gentlemen prof. Ing. Vladimír Šebesta, CSc., doc. Ing. Roman Maršálek, Ph.D., Univ.Prof. Dipl.-Ing. Dr.techn. Markus Rupp and Ing. Jan Prokopec, Ph.D. Last but not least, my great thanks belongs to my family.

The described research was performed in laboratories supported by the SIX project; the registration number CZ.1.05/2.1.00/03.0072, the operational program Research and Development for Innovation.

Contents

List of Figures

List of Tables

Chapter 1

Introduction

At present, the demand for higher data rates in the mobile communications business is still rapidly increasing. Therefore, a huge effort is given into research of new wireless access schemes. To go along with this endeavor, the NTT DoCoMo presented a new wireless access scheme named VSF-OFCDM employing two dimensional (2D) spreading of a transmitted signal [13].

In fact, such a system can be seen as a combination of Orthogonal Frequency Division Multiplexing (OFDM) and CDMA with additional complexity consisting from the application of the 2D signal spreading and deciding how the variable spreading factor will be divided between the time and frequency domain.

To comprehensively describe principles and features of VSF-OFCDM, the reader should be familiar with foregoing technologies:

- CDMA was developed by the military as a communication system resistant to jamming and monitoring, however CDMA can also be used as a channel access method similarly to the frequency or the time domain multiple accesses. This feature of the channel access is nowadays the main highlight of CDMA used in the Universal Mobile Telecommunications System (UMTS) and e. q. in Global Positioning System (GPS).
- OFDM with its orthogonal subcarriers is a popular modulation scheme and has been known since the 70's. Nevertheless, due to high computational requirements of the Fourier transform, it is only used in relatively new standards (e. g. Asymmetric Digital Subscriber Line (ADSL), LTE or Digital Video Broadcasting – Terrestrial (DVB-T)).

From the early nineties, an idea to combine both techniques, the CDMA and OFDM, has been progressively increasing its significance. As a result, several variants of the combination have arisen, for example: Multi Carrier (MC) CDMA or Direct Sequence (DS) CDMA. However, the most promising and advanced ap-

proach seems to be the VSF-OFCDM system proposed by NTT DoCoMo in 2001 [13, 14, 15, 16].

The following text deals not only with the theory of VSF-OFCDM but also with two proposals and comparison of channel estimation methods which are suitable for the VSF-OFCDM system as well as the Peak to Power Ratio (PAPR) reduction method which is needed for successful implementation in real world hardware.

The idea of incorporating of the VSF-OFCDM system as a wireless access scheme for the downlink part of LTE [17] will also be given. The LTE simulator [18] developed at TU Wien was chosen as an appropriate platform for testing and evaluating of the 2D spreading based technology, the comparison with current approaches is thanks to the simulator [19], possible. The simulator contains for example Cyclic Redundancy Check (CRC), turbo coder and rate matcher with Modulation and Coding Scheme (MCS) corresponding to the LTE standard as well as, interlaever and every feature of LTE or another modern wireless communication scheme.

Part I

State-of-the-art

Chapter 2

Issues of modern communication systems

This chapter serves as a brief provider of information about a couple of main wireless channel features which significantly affects modern wireless communication systems which will be frequently discussed in the following text. This chapter also touches issues of designing current wireless communication systems such as the PAPR or Inter Symbolic Interference (ISI) and Inter Carrier Interference (ICI).

2.1 Multipath propagation

Multipath propagation occurs when a transmitted electromagnetic wave reaches the receiving antenna by at least two paths [15]. This is caused by obstacles in the path of the wave, for example by buildings, mountains or even the ionosphere at certain frequencies. Reflected replicas of the transmitted wave then arrive to the transmitter in a different period of time. As a result, when such reflected waves are summed together in a constructive or destructive manner, deep fades often appear. These fades are bounded with the frequency of the electromagnetic wave, velocity of the moving receiver, transmitter or the reflectors as well as the incident angle. Such a situation is depicted in Figure 2.1 where the incident angle is marked as the ϕ, the line-of-sight wave is marked with *1* and the reflected waves are *2* and *3* and v is the velocity of the moving receiver.

2.2 Doppler shift

When the receiver and the transmitter relatively moves to each other, Doppler shift arises as described by Equation 2.1 [14]

$$f_D = \frac{v f_c}{c} cos\phi, \tag{2.1}$$

where v is the relative velocity, c is the speed of light and ϕ is the incident angle as also shown in Figure 2.1.

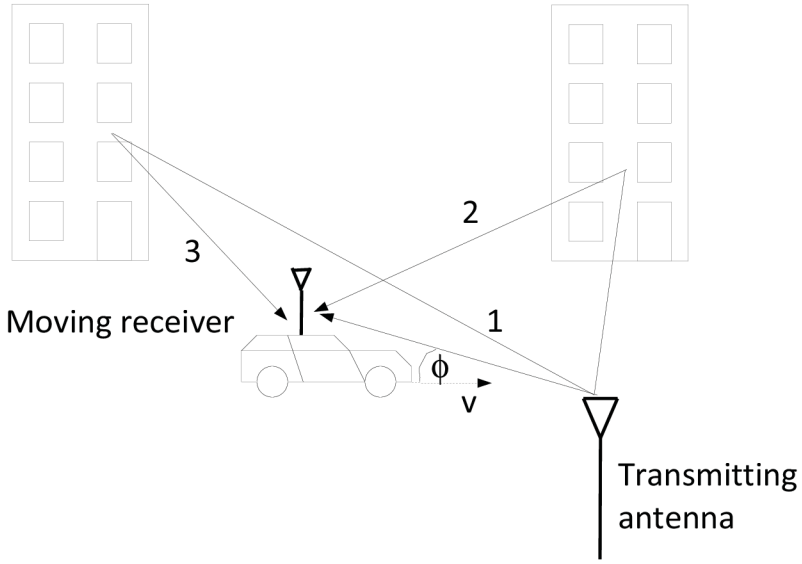

Fig. 2.1: Multipath propagation scene with moving receiver of velocity v, two static reflectors (buildings) and incident angle ϕ.

As a result of the Doppler shift combined with the multipath propagation, the frequency of the transmitted signal spreads. This is referred to as the Doppler spread and its bandwidth is described in Equation 2.2

$$f_{Dmax} = \frac{v f_c}{c} = \frac{v}{\lambda}. \tag{2.2}$$

2.3 Frequency and time selective channel

The attenuation of a wireless channel changes with time and frequency. This phenomenon represents the time-frequency coherence. The coherence bandwidth is defined as:

$$(\Delta f)_c \approx \frac{1}{\tau_{max}}, \tag{2.3}$$

where τ_{max} corresponds to the maximal delay of a signal in the multipath environment. In brief, the time coherence is a time interval where the transfer function of the channel is approximately constant. The coherence time is defined likewise:

$$(\Delta t)_c \approx \frac{1}{2f_{Dmax}}, \tag{2.4}$$

where f_{Dmax} describes the maximal Doppler frequency.

An overall bandwidth of a considered wireless system needs to be taken into account. When exploiting a low-speed narrow-bandwidth system with large symbol durations, the time-frequency coherence can by much larger, thus with no effect on the transmitted data at all.

If we consider a wireless system and a multipath propagation, the system suffers from receiving delayed replicas of the transmitted signal. This is referred to as a delay spread. To cope with the delay spread, the CP concept has bees developed and it is described in the next section.

2.4 Inter symbolic and inter carrier interferences

If considering an up to date multicarrier system, ICI and ISI represents a serious issue. Mainly due to an effort to save valuable spectral space, the subcarriers are placed as close to each other as possible. However, the wireless channel is often rather adverse environment. The subcarriers are affected by the Doppler shift and multipath propagation in an unequal manner. Consequently, the subcarriers may more or less overlap. This effect is referred to as ICI [20, 15].

ISI arises when a large delay spread occurs. A symbol being carried by the line-of-sight path is interfered by a foregoing symbol which is being carried by reflected paths.

2.5 Peak to power ratio

This section will describe a challenging issue of many multicarrier wireless systems - we will give an insight on Peak to Power Ratio (PAPR) and its influence on two major drawbacks which high PAPR causes: an Out-of-Band (OOB) radiation and worse bit error ratio.

To precisely control OOB and BER is of crucial importance on overall usability and reliability of all communication systems. Since OFDM uses many orthogonal subcarriers and as is shown in the chapter devoted to OFDM, the complete OFDM signal is formed from a sum of individual subcarriers which are produced by the IFFT operation of a rectangle pulse. This leads to a signal which has a shape

of a *sinc* function with one enormous peak in the time domain. If we sum these signals representing individual subcarriers, we will inevitably obtain a signal with huge PAPR.

A high PAPR value means that we will need to use an expensive Power Amplifier (PA) with a width linear transfer function, otherwise our system will suffer from nonlinear distortion. This would produce OOB radiation which will interfere other users, or it could increase the error rate since the distorted data could not be properly decoded. Another disadvantage is seen in battery powered applications such as cell phones, or Personal Digital Assistants (PDAs). Due to the fact that the PA operates most of the time in a power de-rated mode, the efficiency is considerably lower [15, 20, 21].

Peak to Power Ratio (PAPR) can be computed as is written here [15]:

$$PAPR(x_\tau, \tau) = \frac{\max_{\tau \in \tau} |x_\tau|^2}{E\left\{|x_\tau|^2\right\}}. \tag{2.5}$$

In equation 2.5, the τ is the time index used to represent the successive time variable t and also the discreet time index n. The $\max_{\tau \in \tau} |x_\tau|^2$ indicates the maximal value of power of the signal x and finally $E\left\{|x_\tau|^2\right\}$ denotes the mean value of the signal.

Equation 2.5 is the general expression of PAPR, but [22] shows an alternative equation (2.6) used for computing PAPR in the frequency domain.

$$PAPR\{x^m(t)\} \leq N \frac{\max |X_k|^2}{E\left\{|X_k|^2\right\}}, \tag{2.6}$$

where N is the number of subcarriers. The marking of signals follows the way of marking in Figure 6.10.

Chapter 3

Multicarrier and spread spectrum systems

When compared with conventional singlecarrier systems, multicarrier systems may reach significantly higher data rates in the challenging fading and electromagnetic wave reflecting environment.

In this introduction, we compare two systems: a singlecarrier system and a multicarrier system, both with the same bit rate. When the bit rate increases above a certain limit, the time duration of one symbol in the single carrier system becomes comparable with a delay spread of a propagation environment. This causes ISI which in fact limits the bit rate of the singlecarrier system. While the time duration of one symbol in the multicarrier system is usually larger, the inter symbol interference affects the data rate significantly less.

As we are comparing systems with the same bit rate as stated above, we have N subcarriers to transmit the same amount of data. Thus, the time duration of one symbol is approximately N-times larger. Using a cyclic prefix (will be explained later) then such a multicarrier system effectively copes with intersymbolic interferences which no longer limits the bit rate [14, 15, 20].

3.1 Orthogonal Frequency Division Multiple Access

OFDM is a specific type of multicarrier modulation technique with orthogonal subcarriers. Thanks to its orthogonality, the conventional frequency guard band is omitted in order to save the frequency spectrum. This is shown in Figure 3.1

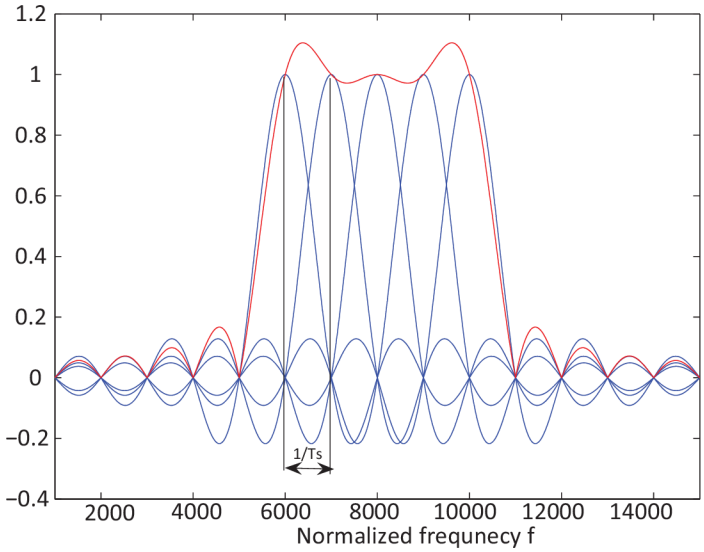

Fig. 3.1: The depiction of orthogonal subcarriers and the time duration of one OFDM symbol.

OFDM modulator

The signal processing in the OFDM modulator is described by equation 3.1.

$$s(t) = \sum_{n=-\infty}^{\infty} \sum_{m=0}^{M-1} a_n^m Rect_T(t - nT) e^{j2\pi m \frac{t}{T}}, \tag{3.1}$$

where m is the subcarrier number, n is the symbol order, a_n^m denotes the n-th symbol transmitted in the m-th subcarrier and finally $Rect_T$ is the rectangular window function with duration of T, which is also defining for the OFDM symbol durability.

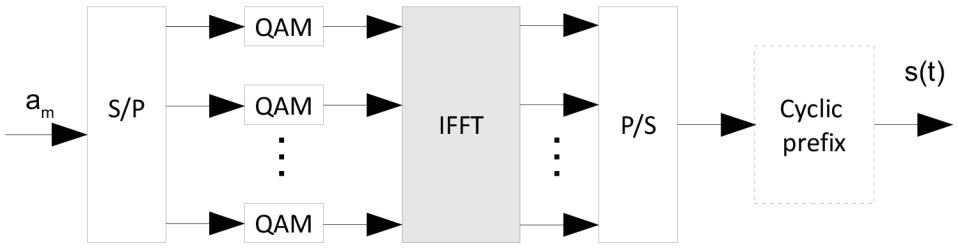

Fig. 3.2: The scheme of the OFDM modem using a QAM inner modulation and cyclic prefix.

Cyclic OFDM symbol extension

As has been stated in the previous paragraph, a delay spread caused by the multipath propagation is a serious issue. By adopting a guard time, when no signal is transmitted at all, we effectively cope with the delay spread and thus the ISI is suppressed.

However, to deal with the ICI as well, an end part of the transmitted signal has to be cyclically copied at the beginning of the signal, as is shown in Figure 3.3 [15]. Thus, the orthogonality of transmitter subcarriers is maintained and the ICI is inhibited as well as the ISI.

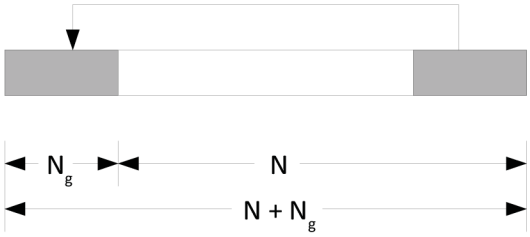

Fig. 3.3: Stylized plot of the way how the CP principle operates.

3.2 CDMA

The main idea behind the military developed Code Division Multiple Access (CDMA) is in spreading the transmitted signal in the frequency domain and so hiding the transmitted signal under the noise floor and as a result to preventing unwanted detection. This is done by multiplying each transmitted symbol by a spreading sequence and thus by increasing transmission rate. This also expands the bandwidth as seen in Figure 3.4.

Nowadays, the CDMA has another advantageous feature. Alongside the Time Division Multiple Access (TDMA) and Frequency Division Multiple Access (FDMA), the CDMA approach enables a completely new kind of multiple access. Namely, the CDMA exploits orthogonal codes in order to accommodate more users in a given time-slot and frequency band.

Spreading process in the CDMA

The rows or columns of a Hadamard matrix can be utilized as the orthogonal spreading sequences. Due to the orthogonality, it is possible to distinguish individual users. The spreading process is depicted in Figure 3.5. The original data of time-duration

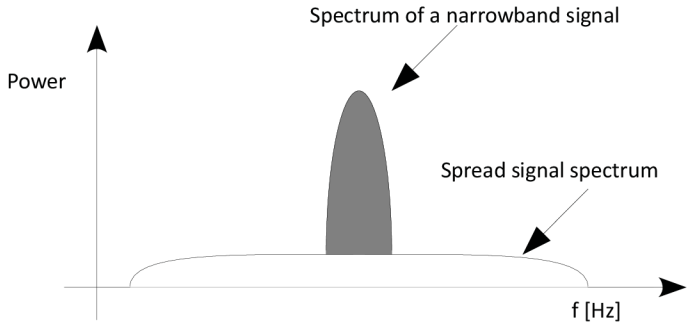

Fig. 3.4: As the symbol time-duration decreases by the effect of multiplying by the spreading sequence, the bandwidth expands.

T_b are multiplied by the spreading sequence c with lower time-duration T_c and as a result the chip stream of spread data is obtained. The data-rate of the resulting chip-stream has to be significantly larger and therefore the bandwidth spreads. By exploiting several codes, several users can be summed in the frequency domain and thus the code multiple access is enabled.

Due to the broad-bandwidth character of CDMA, a very common interference represented by spectrally narrow pulses, affects the CDMA signal rather weakly - especially in comparison with conventional single carrier wireless systems.

Naturally, this method brings difficulties in terms of synchronizing all the users in a time domain or in the power control of each user. However, discussing these topics is beyond the focus of this brief introduction of the CDMA principle.

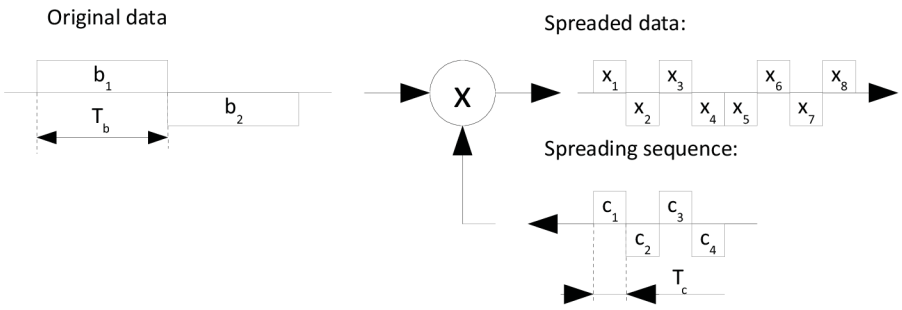

Fig. 3.5: The principal scheme of CDMA spreading. The original data of time-duration T_b are multiplied by the spreading sequence c with lower time-duration T_c and as a result the chip stream of spread data is obtained.

Chapter 4

LTE

In this chapter, we give an insight on the Long Term Evolution (LTE) system, especially in terms of the OFDM based downlink as well as the uplink which utilizes the PAPR minimizing Single-carrier FDMA (SC-FDMA).

We briefly familiarize readers with the LTE standardized features related to the LTE physical layer and the LTE simulator [23]. In the last part of this chapter, a novel two dimensional (2D) signal spreading method, incorporated in the above mentioned LTE link level simulator will be introduced and evaluated.

Link level simulations are needed in order to assess physical layer procedures [19]. In the case of LTE, the new iteration in wireless standards from the 3rd Generation Partnership Project (3GPP), the physical layer is based on Orthogonal Frequency Division Multiple Access (OFDMA), as opposed to UMTS, which was based on Wideband CDMA (WCDMA). The new physical layer offers many advantages, such as high flexibility in bandwidth allocation and not needing complex time-domain equalization such as the one present in WCDMA system. However, it presents new challenges, such as in channel estimation [24], frequency offset correction [25], HARQ modeling [26], or feedback calculation [27].

The following section presents the LTE uplink and downlink link level simulators. While using a similar structure, both the uplink and downlink, the LTE uplink employs SC-FDMA, in contrast with the OFDMA-based downlink. Thus performing differently. Building on top of the base from [28], given the structural similarities between uplink and downlink, which share common blocks such as channel coding, we implemented an uplink counterpart to the simulator presented in [28] based on the 3GPP Release'8 LTE standard [10, 11, 12]. As a second part, we implemented the novel 2D signal spreading method as well as we reveal its performance when compared with standard LTE downlink.

4.1 LTE description

This section provides an insight on the transmitter and the receiver structure of the LTE uplink, as well as the 3GPP LTE standard on which they are based.

4.2 Transmitter

The description of the signal processing of a Transport Block (TB) is given in the following subsection.

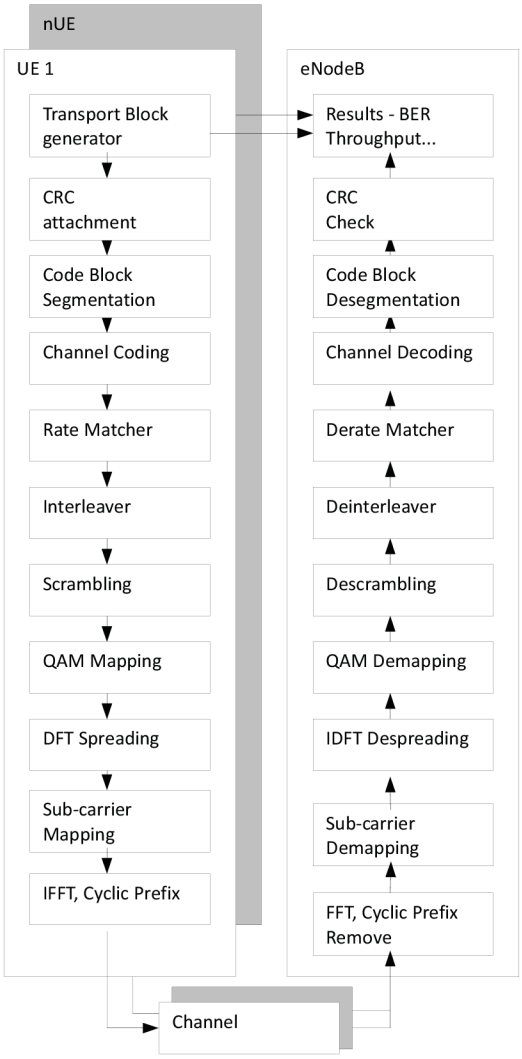

Fig. 4.1: Signal Processing chain used in the LTE uplink link level simulator. Shown blocks are according with [10, 11, 12]

The TB is passed from the Uplink Shared Channel (UL-SCH) transport channel. The physical layer procedures include, as described in [11], a 24-bit TB CRC,

followed by a segmentation in Code Blocks (CBs) due to the finite size of the turbo coder interleaver and CB CRC addition. The output of the segmentation is coded by the 1/3 turbo code subsequently rate-adjusted in the rate matcher. The CBs are finally concatenated and the coded TB is then output. The whole process is depicted in 4.1.

In the next part of this section, we describe our transmitter model, as specified in the 3GPP LTE standard. Firstly, the specific uplink modulation will be presented, then the subcarrier mapping, the LTE time-frequency grid and at the end a short view on the Channel Quality Indicator (CQI).

4.2.1 SC-FDMA modulation

SC-FDMA gets a priority for the LTE uplink before the well known and proved OFDMA due to the effort of minimizing the PAPR in the uplink part of the LTE physical layer. The PAPR was determined critical because of the battery constrain on User Equipment (UE) side as well as a demanding construction of sufficiently linear power amplifiers. [21]

SC-FDMA modulation is based on the OFDM approach. However, a Discrete Fourier Transform (DFT) precoding of the signal is employed. This operation spreads individual subcarriers which are known from the OFDM system over the assigned bandwidth and convert it to a single-carrier transmission, thus effectively reducing the PAPR.

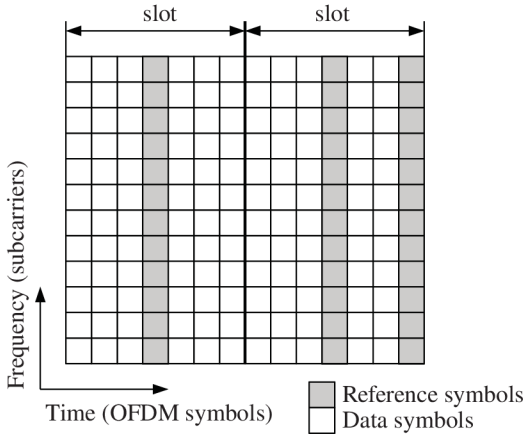

Fig. 4.2: Uplink Time-Frequency grid with reference symbols used in the LTE uplink link level simulator

4.2.2 Subcarrier mapping

A need exists for adding zero subcarriers into the frequency grid in order to achieve appropriate size of the Fast Fourier Transform (FFT) and IFFT operations in the receiver and the transmitter parts respectively. This add operation is driven by a subcarrier-mapping algorithm. In our simulator, the localized mapping is employed. However, besides the localized mapping, there also exists the distributed subcarrier mapping.

The distributed mapping has been examined in literature [20, 29], and simulations showed only a small improvement in terms of BER performance over the localized mapping. However, it is expected that in a real system the performance will be better for the localized mapping due to simpler scanning of the channel transfer function. Moreover, the distributed mapping brings additional complexity to the system, thus the localized mapping is the choice for LTE uplink.

4.2.3 The LTE time-frequency grid

The time-frequency grid of the LTE uplink as well as the downlink consists of so-called Resource Elements (REs). In the time and frequency domain, the grid is divided into 1 ms-long subframes and 180 kHz Resource Blocks (RBs) respectively (see 4.2). The REs are in fact the elementary time-frequency spaces used for transmission of one data symbol from the used constellation diagram (4-, 16-, or 64-QAM). When using 15 kHz subcarrier spacing and normal CP length [10], a RB consists or twelve subcarriers and one subframe of 14 OFDM symbols. For transmission of the reference signals, three OFDM symbols are needed in a subframe. This reference signals are exploited for channel estimation and demodulation purposes.

4.2.4 Channel Quality Indicator

Channel state information is reported by the UE by means of CQI reporting. The four-bit CQI value reports the highest possible MCS from a predefined set that is supported with the current sensed channel conditions while ensuring a Block Error Ratio (BLER) lower or equal to 10%, as in the downlink [12]. The modulation and coding scheme information for uplink is transmitted via the physical control channel in the downlink. Due to this fact, CQI values are utilized for the selection of the modulation order and coding scheme. By the standard definition, the CQI value is calculated on UE side and reported back to the eNodeB.

The CQI value contains in fact two pieces of information: Modulation Order (4-QAM, 16-QAM, or 64-QAM), and the Effective Code Rate (ECR). After the 1/3 turbo coder employed in the LTE uplink, the rate matcher module adjusts the

output ECR to the desired value. The ECR thus describes the level of redundancy after the rate matching operation, as expressed in [30].

The ECR, which is in [10] described as ECR $= 1024\frac{c_R}{e_R}$, where c_R is the number of useful data plus CRC and e_R is the number of output coded bits. The target ECR value is then used for TB size determination. The allowed TB sizes are given in [11], and take into account the modulation order and number of RBs assigned by the system to the UE. Combined with the resource grid size, the maximum number of bits transmitted over the physical layer can be determined.

4.3 Receiver

Signal processing at the receiver is inverse to the transmitter. Firstly, the CP is removed, then the IFFT is calculated and the reference signals are removed. The data is split according to the number of UEs and the assigned number of RBs. At this point, the DFT precoding is removed. Afterwards, the receiver algorithms is called, which currently is implemented via hard demapping. Figure 4.1 depicts the receiver chain, including the complete channel decoding, code block concatenation, and CRC calculation. After decoding the data, BER, BLER and throughput are evaluated.

Part II

Own work

Chapter 5

Aims of the thesis

The dissertation describes the VSF-OFCDM systems, its critical parameters like the two dimensional spreading factor and its dependency on BER considering more transmission channel models, PAPR and its minimization as well as giving proposals of channel estimation techniques especially appropriate for VSF-OFCDM. This could be, in short, summarized as:

- To examine whether the 2D signal spreading could be beneficial in terms of the throughput maximization in modern communication systems.
- Incorporation of the 2D spreading into the LTE physical layer model [19]
- To examine the influence of PAPR and propose a method for its minimization.

To be more specific, the main aim of this work is then to exploit the 2D signal spreading based mainly on the VSF-OFCDM approach [13, 31, 32] as a wireless access scheme in a downlink part of the LTE physical layer simulator [17, 18, 19]. This algorithm brings additional time-frequency diversity. This is beneficial in terms of ability to decode transmitted data in the receiver site, when a multipath fading is considered. The algorithm do not require additional signaling nor extra bandwidth so it brings no extra overhead.

The secondary topics are to examine possibilities of PAPR reduction methods applied directly on VSF-OFCDM. Minimizing PAPR is a popular theme at present and there are a lot of articles about it but not so many about minimizing PAPR related to VSF-OFCDM systems.

Another topic we dealt with is to find out whether the up to date channel estimation principles could also serve in a system exploiting the 2D signal spreading or whether there could be found more appropriate algorithm for the channel state estimation. As a result, one new channel estimation method has been proposed and compared with the-state-of-the-art pilot estimation method.

Chapter 6

VSF-OFCDMA

6.1 Introduction

DATA spreading in the VSF-OFCDM system can be done in two dimensions - in the frequency domain and in the time domain. This is the main difference when comparing the OFDM or the CDMA approaches. The two dimensional Spreading factor (SF) is expressed as:

$$SF = SF_t \times SF_f, \tag{6.1}$$

where SF_t is the spreading factor in the time domain, and SF_f is the spreading factor in the frequency domain.

Variable spreading means that we can change the spreading factor according to current transmission channel conditions to get a lower BER [13].

It was shown in [1] that a proper setting of the spreading factor can reduce the BER and, moreover, to reduce BER, a proper setting of separate SF_t and SF_f parameters is of greater importance than the whole spreading factor SF. This feature monitors the channel coherence bandwidth and channel coherence time.

Figure 6.1 shows the scheme of 2D spreading in the VSF-OFCDM system. At first, a certain number of data symbols are spread by 1D spreading code of length SF. Tor these the Hadamard sequences are used. Consequently, the S/P block is used to divide the data stream from 1D spreader into SF secondary 2D spread data streams according to the desired SF pattern. These streams are the input of the IFFT block which creates the orthogonality between subcarriers. The block named optional interleaver is exploited for minimizing PAPR - this principle is shown for example in [2] [33].

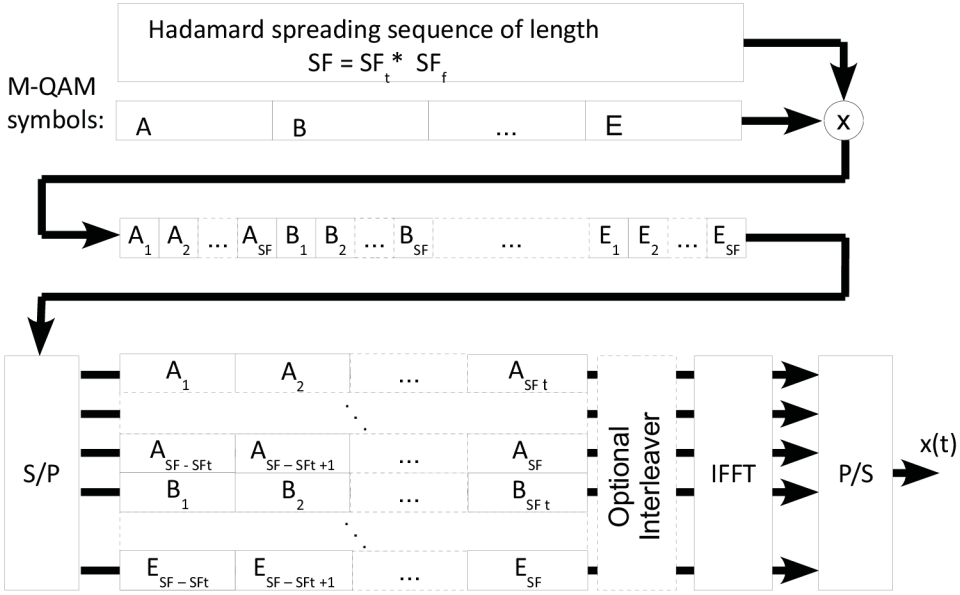

Fig. 6.1: A Scheme of 2D spreading in VSF-OFCDM.

6.2 Transmitter signal processing

The following text will describe the signal processing in the model of two dimensional spreading system, namely VSF-OFCDM. If $\boldsymbol{a}^{x,u}$ is considered as the x-th VSF-OFCDM symbol of the u-th user, then relation 6.2 can be written as:

$$\boldsymbol{a}^{x,u} = \left(a_1^{x,u}, a_2^{x,u}, \ldots, a_k^{x,u}, \ldots, a_{\frac{N}{SF_f}}^{x,u} \right) \tag{6.2}$$
$$\forall k \in \left[1, \frac{N}{SF_f} \right] : a_k^{x,u} \in \{-1, 1\},$$

where x can also be regarded as the VSF-OFCDM frame number graphically expressed in Figure 6.2. An element $a_k^{x,u}$ of VSF-OFCDM symbol $\boldsymbol{a}^{x,u}$ is a Phase Shift Keying (PSK) symbol. It should be noted that the sign marks a vector quantity. The N is the number of subcarriers. The spreading of the symbol $\boldsymbol{a}^{x,u}$ is done according to:

$$\boldsymbol{a}_{\mathrm{s}}^{x,u} = \boldsymbol{a}^{x,u} \otimes \boldsymbol{\xi}^{u}, \tag{6.3}$$

wherein $\boldsymbol{\xi}^{u}$ is the Hadamard spreading sequence of the u-th user, $u \in [0, U]$ or, it can also be regarded as the number of a row or column of the Hadamard matrix,

which has dimensions $SF \times SF$ and each element is from $\{-1, 1\}$. U is the number of code channels. The sign $\otimes$ denotes the Kronecker tensor product.

$$\boldsymbol{\xi}^u = (\xi_1^u, \xi_2^u, \ldots, \xi_{SF}^u)\,. \tag{6.4}$$

After the spreading of the signal, there is a serial into parallel transformation $SP\{.\}\Big|_{N,SF_t \times SF_f}$. The resulting matrix has the numbers of rows and columns equal to N, SF_t respectively, so the exact form of the SP transformation is given by the N and SF parameters and can be expressed as:

$$SP\left\{\boldsymbol{a}_{\mathrm{s}}^{x,u}\right\}\Big|_{N,SF_t \times SF_f} := \begin{pmatrix} a_{\mathrm{s}1}^{x,u}\xi_1^u & \cdots & a_{\mathrm{s}1}^{x,u}\xi_{SF_t}^u \\ \vdots & \ddots & \vdots \\ a_{\mathrm{s}1}^{x,u}\xi_{SF-SF_t+1}^u & \cdots & a_{\mathrm{s}1}^{x,u}\xi_{SF}^u \\ a_{\mathrm{s}2}^{x,u}\xi_1^u & \cdots & a_{\mathrm{s}2}^{x,u}\xi_{SF_t}^u \\ \vdots & \ddots & \vdots \\ a_{\mathrm{s}\frac{N}{SF_f}}^{x,u}\xi_{SF-SF_t+1}^u & \cdots & a_{\mathrm{s}\frac{N}{SF_f}}^{x,u}\xi_{SF}^u \end{pmatrix}. \tag{6.5}$$

The transformed signal is the input of the IFFT operation, the result $\boldsymbol{s}_m^{u,x}$ is considered as a VSF-OFCDM frame.

$$\boldsymbol{s}_m^{u,x} = IFFT\left\{\left\{SP\left\{\boldsymbol{a}_{\mathrm{s}}^{x,u}\right\}_m\Big|_{N,\ SF_t \times SF_f}\right\}^T\right\},\ \forall m \in [1, N]. \tag{6.6}$$

It can be written that:

$$\boldsymbol{s}^{u,x} = \left[\boldsymbol{s}_1^{u,x}, \boldsymbol{s}_2^{u,x}, \ldots, \boldsymbol{s}_m^{u,x}, \ldots, \boldsymbol{s}_N^{u,x}\right], \tag{6.7}$$

where $\boldsymbol{s}^{u,x}$ is a matrix with N columns. These columns are the vectors $\boldsymbol{s}_m^{u,x}$. $\{.\}^T$ indicates the matrix transposition and where:

$$SP\left\{\boldsymbol{a}_{\mathrm{s}}^{x,u}\right\}_m\Big|_{N,SF_t \times SF_f}$$

is the m-th row of the matrix:

$$SP\left\{\boldsymbol{a}_{\mathrm{s}}^{x,u}\right\}\Big|_{N,SF_t \times SF_f}$$

The duration of one VSF-OFCDM frame is denoted T, i.e. $T = \frac{t_{\mathrm{s}}}{SF_t} = \frac{1}{\Delta F}$, where ΔF is the spacing of the subcarriers.

The transmitted signal is, however, a vector quantity and therefore there is a need to transpose the signal $\boldsymbol{s}^{u,x}$ into $\boldsymbol{s}_{\mathrm{PST}}^{u,x}$ signal according to:

$$\boldsymbol{s}_{\mathrm{PST}}^{u,x} := PST\left\{\boldsymbol{s}^{u,x}\right\} = \left(s_{1,1}^{u,x}, s_{2,1}^{u,x}, \ldots, s_{SF_t,1}^{u,x}, s_{1,2}^{u,x}, \ldots, s_{SF_t,N}^{u,x}\right). \tag{6.8}$$

The PST abbreviation indicates Parallel Serial transform in the Transmitter.

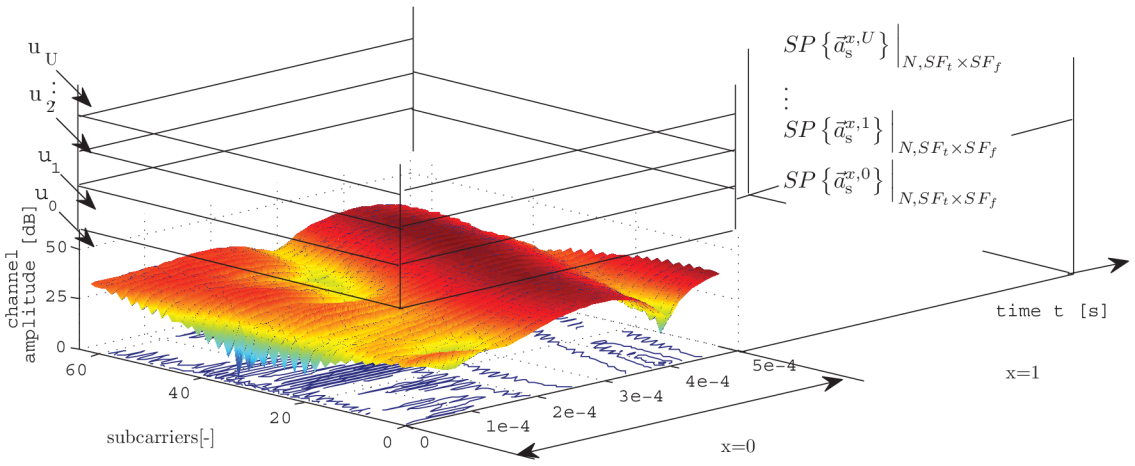

Fig. 6.2: The graphical expression of the data code-channels and the channel-sensing code channel - on the y axis are expressed all the code-sheets, distinguished by $u_{0\ldots U}$

6.3 Receiver signal processing

The signal processing at the receiver side is closely related with currently exploited channel estimation techniques. We propose two channel estimation techniques, therefore the following text is divided into two sections.

6.3.1 Channel Estimation Technique Based on Code Division in VSF-OFCDM

This estimation process uses one $\boldsymbol{a}^{x,u}$ symbol (see equation 6.2) with one exactly specified user superscript u for all frame superscripts x as a training sequence. At the receiver end, the value of $\boldsymbol{a}^{x,u}$ is known exactly. It is meant to be stored in a memory - the value of $\boldsymbol{a}^{x,u}$ is time invariant. The symbol $\boldsymbol{\zeta}$ is a CSI vector and has to be calculated at the receiver for every VSF-OFCDM symbol - every frame number x.

The FFT of the received signal $\boldsymbol{r}$ is firstly calculated at the receiver according to:

$$\boldsymbol{a}_{\mathrm{r}} = FFT\{\boldsymbol{r}\}. \tag{6.9}$$

The signal $\boldsymbol{a}_{\mathrm{r}}$ is transformed:

$$\boldsymbol{a}_{\mathrm{r\,PSR}}^{x,u} = \frac{1}{SF}\sum_{n=1}^{SF}\left\{PSR\{\boldsymbol{a}_{\mathrm{r}}\}\Big|_{\frac{N}{SF_f},SF} \odot \boldsymbol{\Xi}^{u}\right\}_{k,n}, \forall k \in \left[1, \frac{N}{SF_f}\right], \tag{6.10}$$

so it can be written:

$$\boldsymbol{a}^{x,u}_{\mathrm{r\ PSR}} = \begin{bmatrix} a^{x,u}_{\mathrm{r\ PSR}\ 1} \\ a^{x,u}_{\mathrm{r\ PSR}\ 2} \\ \vdots \\ a^{x,u}_{\mathrm{r\ PSR}\ k} \\ \vdots \\ a^{x,u}_{\mathrm{r\ PSR}\ \frac{N}{SF_f}} \end{bmatrix}, \tag{6.11}$$

where $\odot$ is the Hadamard product, and $\{.\}_{k,n}$ denotes the row and column order in the matrix resulting from the Hadamard product. Each row contains all chips of one PSK symbol. The matrix from equation 6.12 has $\frac{N}{SF_f}$ rows. The matrix also has SF columns. The element of the vector $\boldsymbol{a}^{x,u}_{\mathrm{r\ PSR}}$ is one PSK symbol. Finally:

$$PSR\{\boldsymbol{a}_{\mathrm{r}}\}\Big|_{\frac{N}{SF_f},SF} := \tag{6.12}$$

$$\begin{pmatrix} a_{\mathrm{r}\ 1} & a_{\mathrm{r}\ 2} & \cdots & a_{\mathrm{r}\ SF} \\ a_{\mathrm{r}\ SF+1} & a_{\mathrm{r}\ SF+2} & \cdots & a_{\mathrm{r}\ 2SF} \\ \vdots & \vdots & \ddots & \vdots \\ \vdots & \vdots & \cdots & a_{\mathrm{r}\ \frac{N}{SF_f}SF-SF} \\ a_{\mathrm{r}\ \frac{N}{SF_f}SF-SF+1} & a_{\mathrm{r}\ \frac{N}{SF_f}SF-SF+2} & \cdots & a_{\mathrm{r}\ \frac{N}{SF_f}\mathrm{SF}} \end{pmatrix},$$

and the Hadamard despreading matrix:

$$\boldsymbol{\Xi}^u = \left[\{\boldsymbol{\xi}^u_1\}^T, \{\boldsymbol{\xi}^u_2\}^T, \ldots, \left\{\boldsymbol{\xi}^u_{\frac{N}{SF_f}}\right\}^T\right]^T,$$

It should to be noticed that $\boldsymbol{\xi}^u_1 = \boldsymbol{\xi}^u_2 = \cdots = \boldsymbol{\xi}^u_{\frac{N}{SF_f}}$. Then the $\boldsymbol{\zeta}^x$ value, which will contain the channel state information, can be calculated:

$$\zeta^x_k = \frac{a^{x,u}_k}{a^{x,u}_{\mathrm{r\ PSR}\ k}},\ \forall k \in \left[1, \frac{N}{SF_f}\right]. \tag{6.13}$$

Applying CSI:

$$\boldsymbol{a}^{x,u}_{\mathrm{C}} = diag\left\{\{\boldsymbol{a}^{x,u}_{\mathrm{r\ PSR}}\}^T \cdot \boldsymbol{\zeta}^x\right\}, \forall u \in [0, U], \tag{6.14}$$

where $\boldsymbol{a}^{x,u}_{\mathrm{C}}$ denotes a VSF-OFCDM symbol which is corrected by vector $\boldsymbol{\zeta}^x$ containing the CSI. The CSI for the spreading system is not a time-frequency matrix as for pilot-based, but a vector for correcting of despreaded (received) symbols. Because part of the receiver for the spreading system is an integration of chips, the channel information is also integrated and applied after that. The integration also improves

the performance in the Additive White Gaussian Noise (AWGN) channel, and the CSI is relevant even for really low SNR.

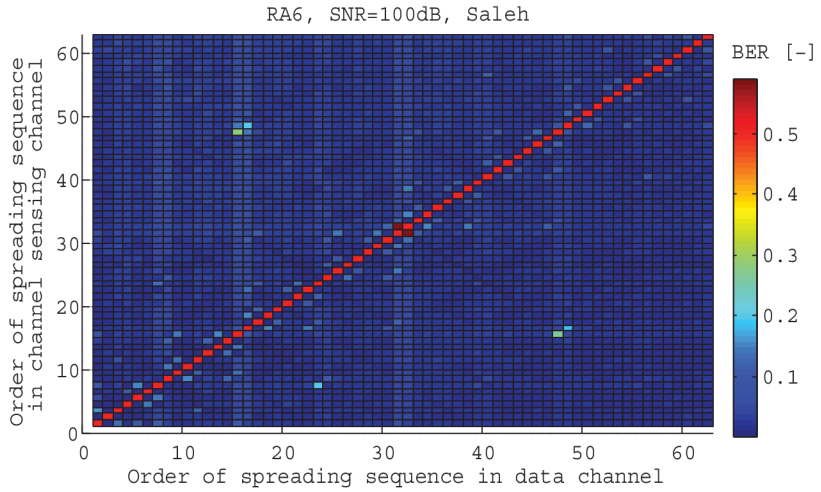

Fig. 6.3: The comparison of spreading sequence usability for estimation purposes and for data transmission.

As one could expect, each Walsh-Hadamard code performs differently in a fading channel environment. Since the estimation channel is of higher priority and is used by all the current users in a serving cell, the Walsh-Hadamard code used for the estimation process is supposed to be the most resistant against the fading effect in a real multipath channel. To follow this reasoning, the comparison of usability of all Walsh-Hadamard codes has been done and the result is depicted in Figure 6.3.

At the x axis we see the order of a spreading code used for data transmission and at the y-axis the order of a spreading code used for the estimation process is placed. The color represents BER. As we see at the diagonal, when the same sequence is used for the estimation as well as for the data transmission, the BER is ≥ 0.5 and as we expected earlier, we see that some sequences are better than others - this should represent a color different from blue.

6.3.2 Pilot Aided Channel Estimation Technique in 2D Spreading Based Systems

The principle of the pilot aided estimation is illustrated in Figure 6.4. Some of the transmitted chips in SP matrix 6.15 are set equal to $\boldsymbol{\zeta}$ 6.16. This information ($\boldsymbol{\zeta}$) is known at the receiver side and therefore the transmission channel influence at the positions of the pilot symbols can be evaluated.

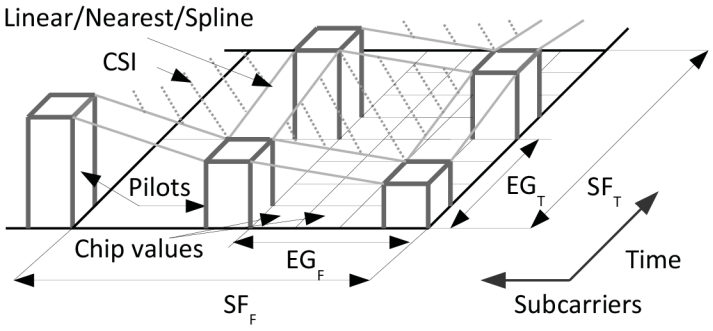

Fig. 6.4: Pilot insertion

If we go back to the transmitter, the pilots are inserted as is expressed in the following, however, firstly we need to decide about the estimation grid in both domains (EG_f, EG_t). It means that the mutual distance of the pilot symbols should be established. The parameter of this decision should be for example the CQI.

$$SP\left\{\boldsymbol{a}_{\mathrm{s}}^{x,u}\right\}\Big|_{N,SF_t\times SF_f} = \begin{pmatrix} a_{\mathrm{s1}}^{x,u}\xi_1^u & \cdots & a_{\mathrm{s1}}^{x,u}\xi_{SF_t}^u \\ \vdots & \ddots & \vdots \\ a_{\mathrm{s1}}^{x,u}\xi_{SF-SF_t+1}^u & \cdots & a_{\mathrm{s1}}^{x,u}\xi_{SF}^u \\ a_{\mathrm{s2}}^{x,u}\xi_1^u & \cdots & a_{\mathrm{s2}}^{x,u}\xi_{SF_t}^u \\ \vdots & \ddots & \vdots \\ a_{\mathrm{s}\frac{N}{SF_f}}^{x,u}\xi_{SF-SF_t+1}^u & \cdots & a_{\mathrm{s}\frac{N}{SF_f}}^{x,u}\xi_{SF}^u \end{pmatrix}. \tag{6.15}$$

Now we need to insert pilot symbols into the SP matrix. We can write:

$$\begin{aligned} \psi_{i,j} &= \zeta \\ \forall i &\in \{1, EG_f + 1, 2(EG_f + 1), \ldots, N\} \\ \forall j &\in \{1, EG_t + 1, 2(EG_t + 1), \ldots, SF_t\}. \end{aligned} \tag{6.16}$$

For applying the CSI, there is a need to interpolate the CSI matrix to the size of the Serial to Parallel (SP) matrix. There methods are used: Linear, Nearest and Spline (see fig. 6.4). Applying of the interpolated CSI matrix is done by performing a multiplication operation - the interpolated CSI matrix is multiplied element-by-element with the matrix of the received signal. The difference between perfect knowledge of channel state information (real state of the channel) and channel state information estimated from pilot subcarriers can be seen in Figure 6.5a and Figure 6.5b.

The performance for different interpolation methods for CSI estimation is shown in Figure 6.6. Simulations are also made for three types of non-linear channel models.

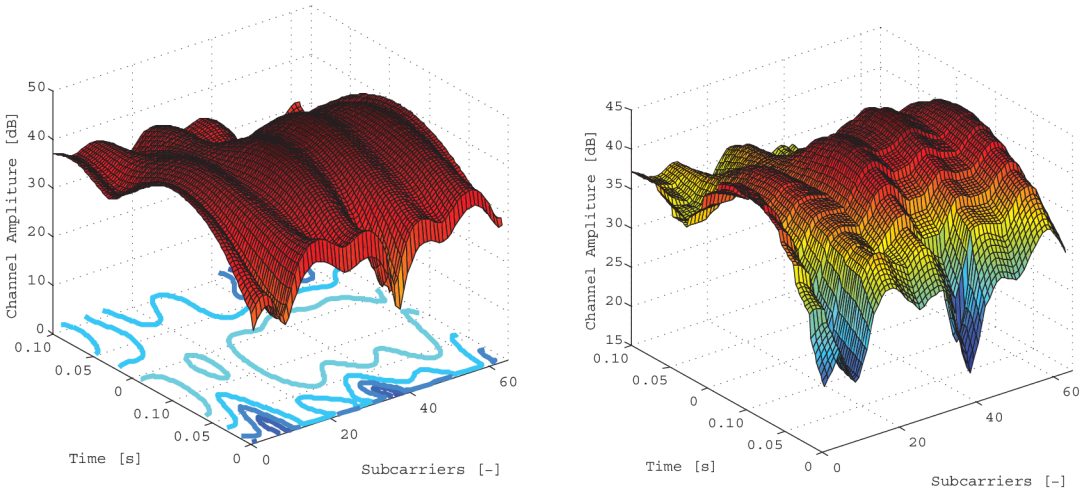

(a) Real CSI matrix (perfect knowledge of the channel state).

(b) Interpolated CSI matrix, method: Nearest.

Fig. 6.5: The CSI matrices

The nearest method for pilot subcarriers interpolations is not recommended. The linear and spline methods almost have the same performance for a selected system, but linear is easier to implement. The VSF-OFCDM system with CSI estimation has better performance in channels with a smaller delay spread (Extended pedestrian channel model (EPA), EVA) as suspected.

Results and conclusions

First of all Table 6.1 with parameters of the proposed system is given. The 2D spreading factor is static in this case; however, this is considered to be variable. For example according to channel conditions, but this feature is disrupting in this attempt so its influence is not examined.

Spreading Factor SF	64
Spreading Factor - freq. domain SF_f	8
Spreading Factor - time. domain SF_t	8
Sample time t_s	5 μs
Number of subcarriers N	128
Modulation method	QPSK
Upsampling in IFFT	8

Tab. 6.1: Parameters of the VSF-OFCDM system model.

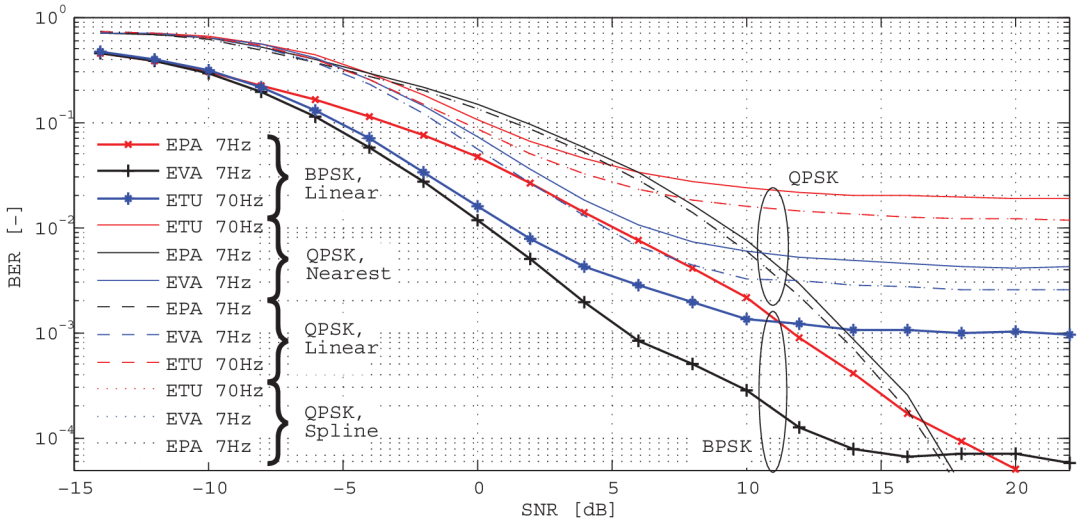

Fig. 6.6: The comparison of BER performance for different interpolations methods for CSI estimation, different channel models and BPSK and QPSK inner modulation of the VSF-OFCDM.

In this section, we have proposed a novel application of the pilot-based channel estimation and CSI interpolation in VSF-OFCDM systems as well as an estimation technique based on code division. The unaffected throughput is the main advantage of our pilot-based channel estimation method. Comparing the overhead information added due to the estimation, the code based method exploits the $1/SF$ part of the transmitted data (one spreading sequence is used). For the simulated system, this corresponds to 1/64, so from 64 transmitted symbols, one is used for estimation. In the case of the pilot based estimation, this is dependent on the pilot sub-carriers grid. For the presented results, the grid was set to 4×4 and this overhead corresponds to 4/64. Therefore, the simulation with the code based estimation method suffers from lower information overhead compared with the pilot based method.

The comparison of a pilot based estimation technique and the proposed method exploiting code division is depicted in Figure 6.7.

We see better performance for the code based estimation system. For our settings $SF = 8 \times 8$, to achieve the same BER level $BER = 10^{-3}$, we need up to 10 dB higher SNR for the pilot based system.

The Doppler effect has been stimulated too and as we can see from Figure 6.7, the code-base estimation system hits an error floor when using maximal Doppler frequency 2 Hz. This is not the case of the pilot based system where we do not observe any error floors.

Figure 6.8a shows the CSI matrix of a pilot-based estimation system for $SNR = 1000$ dB [3]. We can see a rounding error due to the type of interpolation method

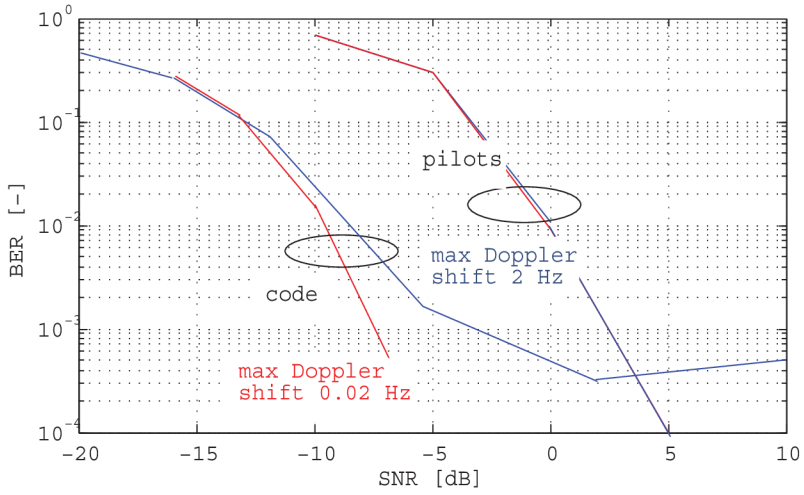

Fig. 6.7: The estimator performance analysis, $SF = 8 \times 8$, $N = 128$, EVA, QPSK - Comparison for the pilot-based and code-based approach. Doppler spread influence.

'nearest neighbor'. A more advanced method could be used, but it will not provide much better results.

In this particular case, the $SNR = 1000$ dB. Pilots are not affected by noise and as a result, the shape of the surface could represent a channel matrix well. Another case is, when the SNR drops to a lower level. In Figure 6.8b we see a degradation of the CSI matrix. The pilot symbols are damaged by a noise and as a result we suffer from poor CSI quality.

If we use the code-based estimation, the CSI matrix for $SNR = 1000$ dB is very similar to the CSI matrix for $SNR = 0$ dB. Here the averaging effect comes into account. The CSI matrix is created after de-spreading and summing. If the AWGN is exploited in our system, its mean value equals zero, so if the SF is high enough, CSI will not be degraded.

Channel model

The transmission channel model in this case is expressed by its impulse response which is given by the International Telecommunication Union (ITU). This is represented by the sampling of Wide-Sense Stationary Uncorrelated Scattering (WSS-US) and by a Doppler shift: [34]

$$h(p,m) = \lim_{R\to\infty} \frac{1}{\sqrt{R}} \sum_{r=1}^{R} e^{(\phi_r + 2\pi f_{D_r} T_s p + 2\pi\tau_r \Delta F m)}, \tag{6.17}$$

where p and m are two characteristics of the process (e.g. time/frequency). There are R echos superposed incoherently. Each path is desribed by a random Doppler

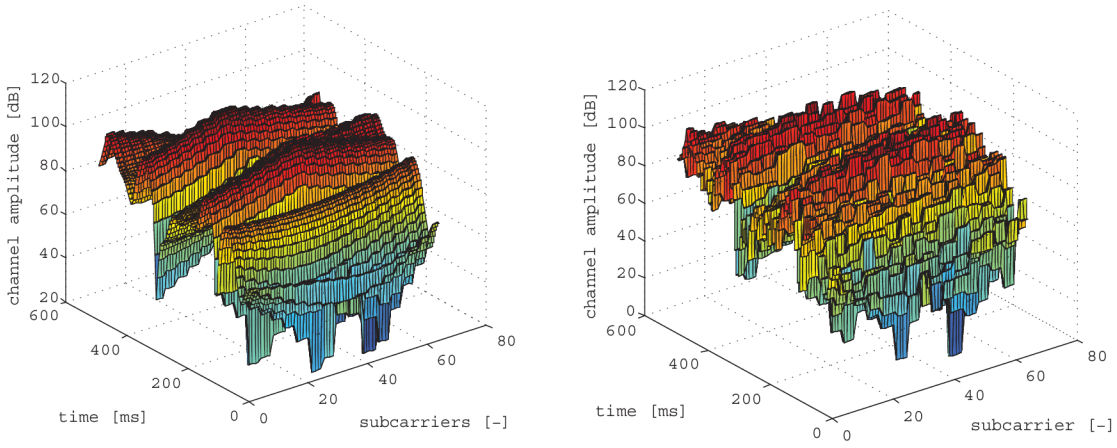

(a) The CSI matrix from pilot-based estimator, $SNR = 1000$ dB

(b) The CSI matrix from pilot-based estimator, $SNR = 0$ dB

Fig. 6.8: Noise influence on the pilot-based generated CSI matrices

shift f_{Dr}, random phase ϕ_r, and random delay τ_r, where $1 \leq r \leq R$. [34]

These are the channel models used:

- EPA, Extended Pedestrian, r.m.s. delay spread = 43 ns
- EVA, Extended Vehicular, r.m.s. delay spread = 357 ns
- ETU, Extended Urban, r.m.s. delay spread = 991 ns

They simulate the environment with low, medium and high (respectively) delay spread and a low (7Hz for EPA and EVA) and medium (70Hz for Extended typical urban channel model (ETU) Doppler shift. The channels have been proposed for in the LTE performance evaluation and therefore the frequencies are around 2.5GHz. [17]

If we compare this code based method with the state-of-the-art pilot based method, also using the VSF-OFCDM simulator, we see that the new method benefits from notably lower BER. This is true for very low Doppler shifts, as the Doppler shift goes up, the code based method reaches an error floor faster than the pilot based method.

Bibliography of author's publications related to stated chapter:

[1] J. Blumenstein and Z. Fedra, "The characteristics of the 2d spreading based communication systems," in *Radioelektronika, 2009. RADIOELEKTRONIKA '09. 19th International Conference*, april 2009, pp. 279 –281.

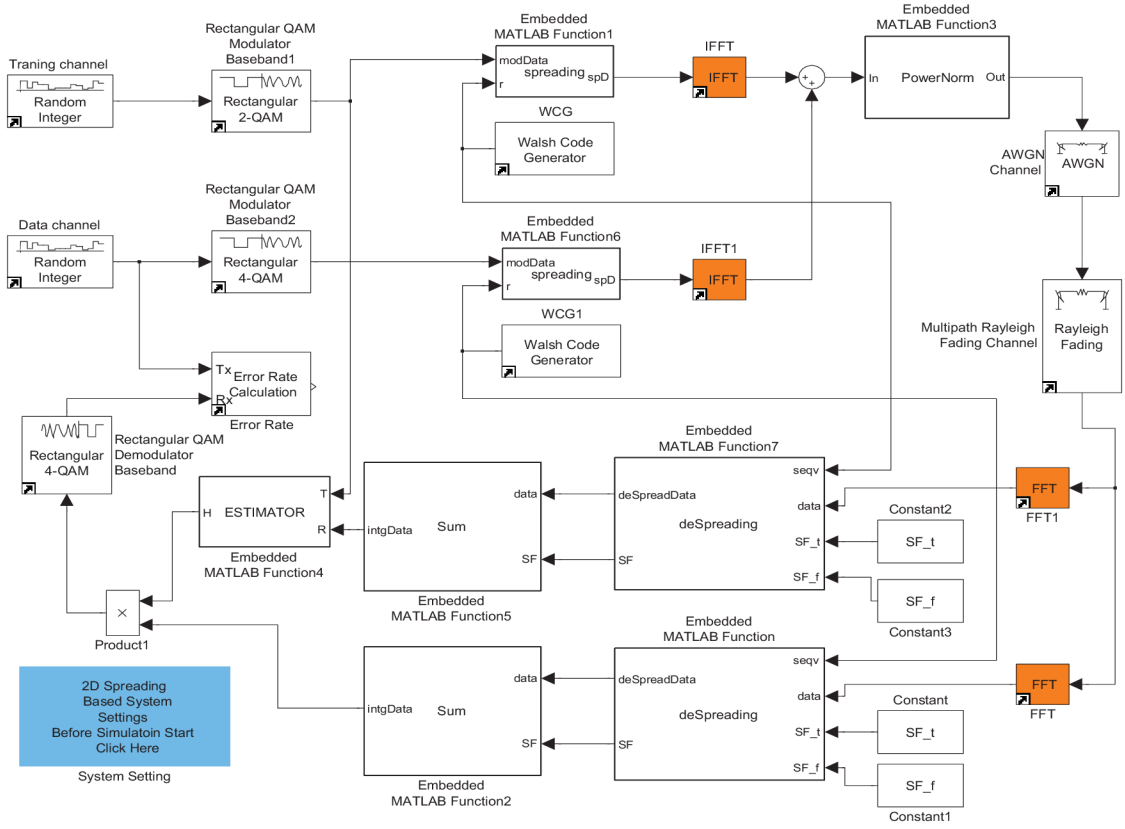

Fig. 6.9: The VSF-OFCDM system model from Simulink. Thanks to embedded Matlab functions we achieve flexibility while lucidity of a block scheme maintained.

[3] J. Blumenstein, Z. Fedra, and V. Šebesta, "Performance of pilot aided channel estimation technique in 2d spreading based systems," *Radioengineering*, vol. 19, pp. 507–510, 2010.

6.4 PAPR minimizing technique in the 2D spreading based system

This section will describe a challenging issue of many multicarrier wireless systems - we will give an insight on Peak to Power Ratio (PAPR) and its influence on two major drawbacks which high PAPR causes: an OOB radiation and worse bit error ratio.

To precisely control OOB and BER is of crucial importance on overall usability and reliability of all communication systems. Since OFDM uses many orthogonal subcarriers and as is shown in the chapter devoted to OFDM, the complete OFDM signal is formed from a sum of individual subcarriers which are produced by the IFFT operation of a rectangle pulse. This leads to a signal which has a shape

of a *sinc* function with one enormous peak in the time domain. If we sum these signals representing individual subcarriers, we will inevitably obtain a signal with huge PAPR.

A high PAPR value means that we will need to use an expensive PA with a width linear transfer function, otherwise our system will suffer from nonlinear distortion. This would produce OOB radiation which will interfere other users, or it could increase the error rate since the distorted data could not be properly decoded. Another disadvantage is seen in battery powered applications such as cell phones, or PDAs. Due to the fact that the PA operates most of the time in a power de-rated mode, the efficiency is considerably lower.

There are numerous methods for minimizing PAPR. A wide overview could be found in [22], or [17]. The problem of minimizing PAPR in a proposed VSF-OFCDM system is that by exploiting the 2D spreading, the system suffers from a much higher PAPR than a proper OFDM [2]. This issue is, however, solved using a simple PAPR minimizing technique, which is based on random interleaving of the IFFT input. A more detailed description with intention to the VSF-OFCDM is to be found in the next sections or application of the interleaving PAPR minimization technique to the Multi-Carrier Code Division Multiple Access (MC-CDMA) as described in [33].

6.4.1 Interleaving method for PAPR minimizing

The principle of the interleaving method for minimizing PAPR is as follows. The data stream of OFDM systems in the time domain can be considered as the sum of sinusoids and when the peak values of these sinusoids are optimally and mutually shifted, the sum of these peaks in one timeslot (and also PAPR parameter) is reduced. It has been shown in [33] that the optimal interleaving pattern gives almost the same results as the random pattern which is used here and can be generated as a random permutation of a number of interleaved chips.

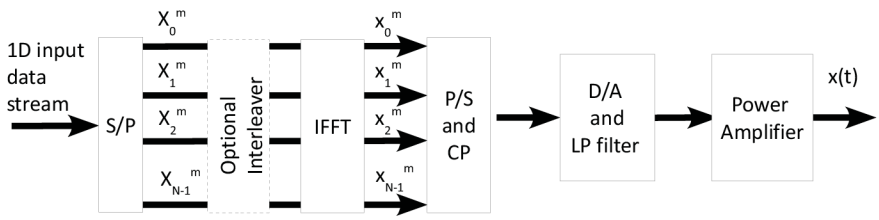

Fig. 6.10: An OFDM transmitter, signal marking

To illustrate this effect, we can observe, in Figure 6.11, a matrix of 2D spread and an interleaved signal just after IFFT operation. The simulated system was

8×4, $N = 32$. The frequency domain is placed on the x axis, the time domain on y axis and finally power of the 2D signal on the z axis. It is clear from Figure 6.11 that one 16-QAM symbol is spread according to the desired spreading pattern, on 4 subcarriers and on 8 timeslots.

The values within the frame of one 16-QAM symbol in the direction of the x and y axes are not the same due to random interleaving and in the direction of the x axis due to the IFFT operation.

The optional random chip interleaving block is used for reducing PAPR as was proposed in [33].

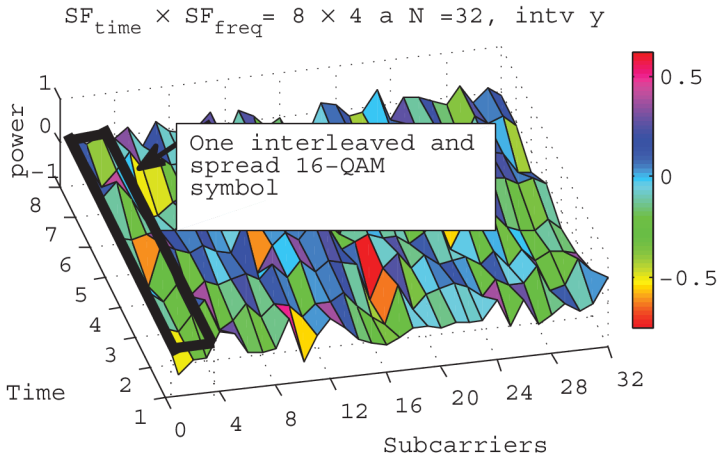

Fig. 6.11: A 2D spread signal after the IFFT operation

PAPR in VSF-OFCDM systems can be observed in two dimensions; in the time and frequency domain. Considering that the main drawback of high PAPR is the increase of BER and OOB radiation caused by nonlinearity of the power amplifier, then the time domain PAPR has more real usage than the PAPR parameter in the frequency domain.

The reason for this is obvious from Fig. 6.10 - we consider the time domain just behind the IFFT block and behind this block the power amplifier is inserted as well. The PAPR is critical for this block.

A numerical example of PAPR values in the frequency domain for 16-QAM modulation is demonstrated in Table 6.2.

Results and conclusions

Results of the simulations are shown in Figures 6.12, 6.13 and 6.14. PAPR was tested in the time domain and the influence of changing SF_{time}, SF_{freq} and N, which represents the number of subcarriers, was observed.

	$PAPR_f$ [dB]	SF patterns
N=80	16,81	10×8
N=160	19,82	20×4, 10×8
N=320	22,83	80×4, 40×8, 20×16
N=640	25,84	640×1, 80×8, 40×16
N=1280	28,85	640×2

Tab. 6.2: $PAPR_f$ [dB] values for 16-QAM modulation and various SF patterns.

The left part of Figure 6.12 shows the Complementary Cumulative Distribution Function (CCDF) of PAPR for 16-QAM. SF_{freq} stays const., $SF_{time} = [8, 16, 32, 64]$ and $N = 120$. Interleaver was not used. PAPR is not significantly rising with increasing of SF_{time}. The reference curve for a pure OFDM system is illustrated in every figure for comparison. The OFDM in this figure has significantly lower PAPR than 2D spreading based systems.

The right part of figure 6.12 shows the situation when $SF_{time} = 10$, $SF_{freq} = [10, 20, 40, 80]$ and $N = 160$. Interleaver was also not used. PAPR is rising with rising SF_{freq} and is rising with N as well. It is shown in the left part of figure 6.13.

The right part of Figure 6.13 illustrates the influence of random chip interleaver. A 16-QAM, $SF = 8 \times 16, N = 1600$ system is considered. We can observe huge reduction of PAPR up to 9dB. The system with an interleaver achieved nearly the same PAPR as the OFDM system with the same number of subcarriers N.

In Figure 6.14, the amplitude histograms of the transmitted signal are plotted for $SF = 16 \times 10$ settings and the interleaver is on and off respectively. The distribution of the amplitudes of systems with an interleaver is close to the Rayleigh distribution as well as the OFDM system. If no interleaver is used, the distribution is exponential.

This section gave an insight onto the VSF-OFCDM system with time-frequency spreading and its performance of PAPR with different 2D spreading patterns.

An important conclusion is that PAPR is not growing with growing SF_{time}, but with SF_{freq} and with N PAPR is growing significantly. This feature can be profitably used in designing various SF patterns in VSF-OFCDM systems. Last but not least we have shown that PAPR can be simply and effectively reduced nearly to the OFDM PAPR level [2, 4].

6.4.2 High PAPR and PA nonlinearities

As has been stated in the previous sections, considering the PA nonlinearities, high PAPR value affects the BER and OOB radiation. To examine this effect, we developed the VSF-OFCDM simulator [5]. This simulator is done in Matlab and

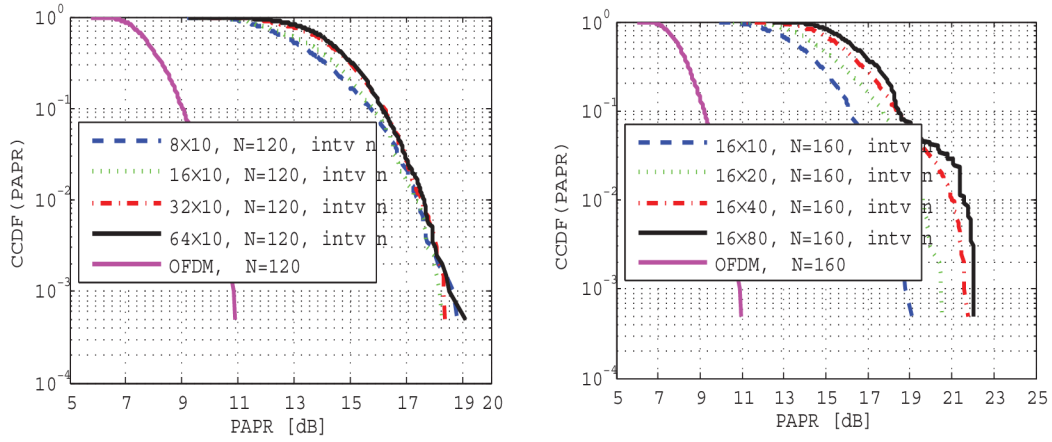

Fig. 6.12: CCDF of PAPR for 16-QAM, in the left fig. SF_{freq} stays const., $SF_{time} = 8, 16, 32, 64$ and $N = 120$. An interleaver was not used . The right fig. $SF_{time} = 10$, $SF_{freq} = [10, 20, 40, 80]$, $N = 160$. Interleaver was not used.

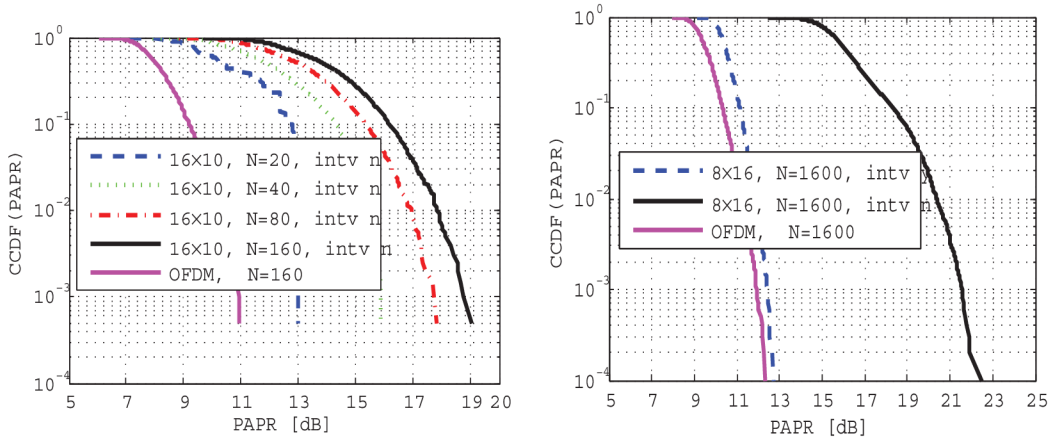

Fig. 6.13: CCDF of PAPR for 16-QAM, in the left fig. $N = [20, 40, 80, 160]$ and $SF = 16 \times 10$. Interleaver was not used. In the right fig. shows the influence of an interleaver on 16-QAM $SF = 8 \times 16, N = 1600$ system.

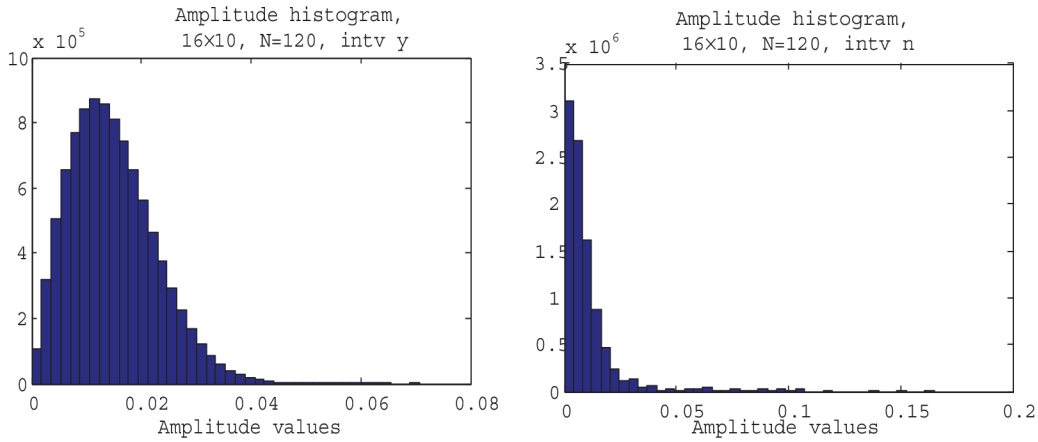

Fig. 6.14: Amplitude histograms of $SF = 8 \times 16, N = 120$ systems. The left with an interleaver, right without an interleaver.

Simulink, it is free of charge for academic usage and is downloadable from [5].

Bit error ratio experiment

To simulate real PA, we choose the Saleh nonlinearity [35] for its simplicity, widespread and common usage. It is fully described by two parameters:

The AM/AM parameters, alpha and beta, are used to compute the amplitude gain for an input signal using the following function:

$$F_{AM/AM^{(u)}} = \frac{\alpha u}{1 + \beta u^2}, \tag{6.18}$$

where u is the magnitude of the scaled signal. The AM/PM parameters, alpha and beta, are used to compute the phase change for an input signal using the following function:

$$F_{AM/PM^{(u)}} = \frac{\alpha u^2}{1 + \beta u^2}, \tag{6.19}$$

where u is the magnitude of the input signal. Note that the AM/AM and AM/PM parameters, although similarly named alpha and beta, are distinct [36].

For our attempt, the parameters have been chosen: AM/AM = [2.1582 1.1547], AM/PM = [4.0033 9.1040]. The input/output characteristic is in Figure 6.15c.

Another way to show the nonlinearity influence is to use the histogram from Figure 6.15 where on the x axis is the amplitude value and on the y axis will be placed the number of occurrences in the signal vector. If comparing the histogram before the Saleh nonlinearity 6.15a and the histogram after the Saleh model of a PA 6.15b, we could easily see the paramount influence of such a nonlinearity. It is worth mentioning that all the amplitudes greater than 1 from Figure 6.15a are after the Saleh nonlinearity rounded to 1. It has to simulate that the PA is saturated when amplitudes are equal to 1 and has no more power to amplify amplitudes of higher power. A huge reshuffle of energy occurs in the frequency domain as well as a distortion of the signal in such a way that proper demodulation of a quadrature amplitude modulated signal of some higher state (16-QAM or 64-QAM) is rather challenging.

In the next figure, 6.16, we see the scheme produced by the VSF-OFCDM simulator [5]. The signal processing strictly follows the description given in section 6.1 and the current setting is: $SF = 8 \times 8$ and $SF = 16 \times 16$ - we tried to examine whether the spreading factor affects the overall PAPR of the VSF-OFCDM system and as a result also the BER and OOB radiation. It needs to be stated that also the order of Walsh-Hadamard sequence used for the signal spreading has its influence as is shown in Figure 6.3.

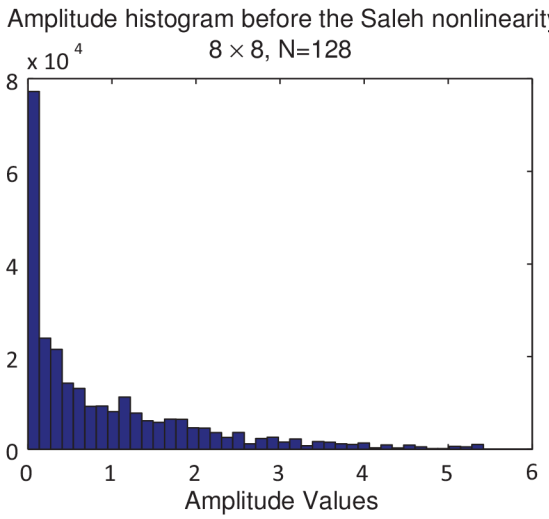

(a) The amplitude histogram of the signal before the Saleh nonlinearity

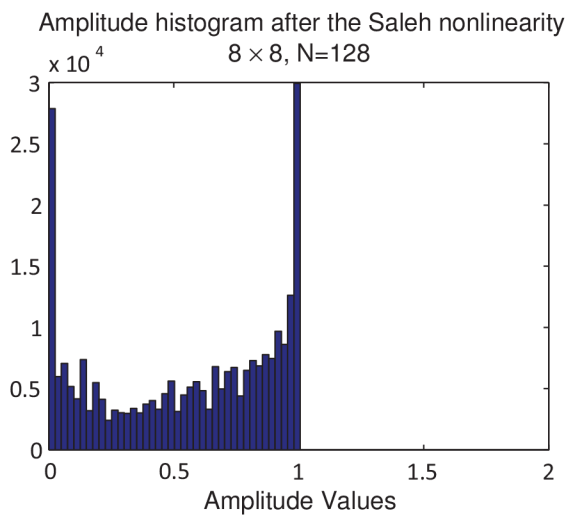

(b) The amplitude histogram of the distorted signal

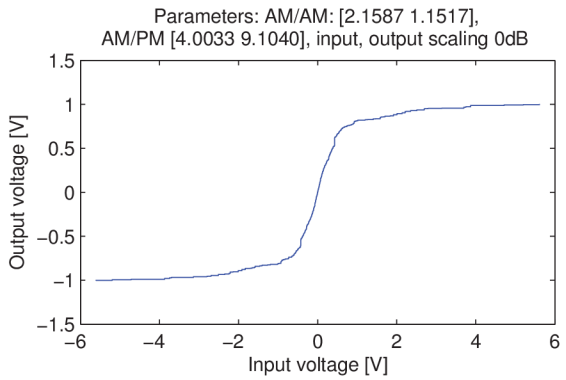

(c) BER performance and a Saleh nonlinearity input/output curve

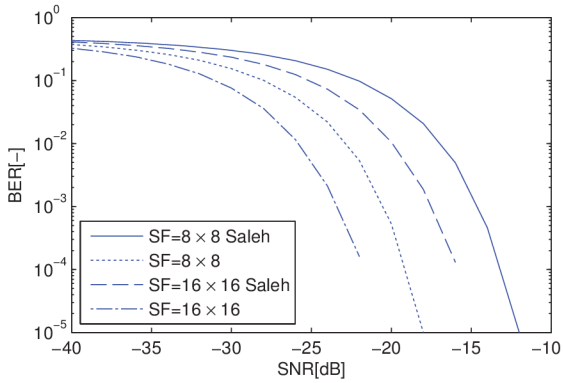

(d) The BER performance and comparison of the VSF-OFCDM system with PA modeled by the Saleh nonlinearity and ideal PA

Fig. 6.15: Noise influence on the pilot-based generated CSI matrices.

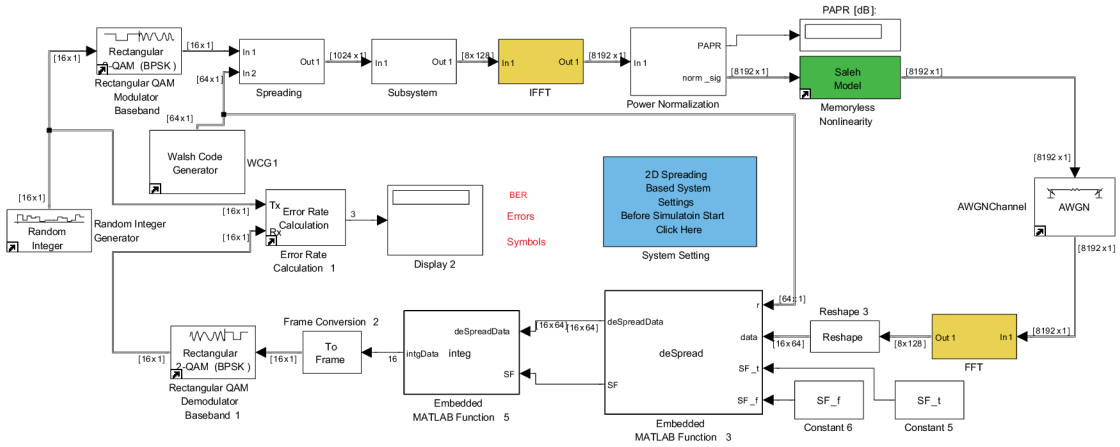

Fig. 6.16: The VSF-OFCDM simulator when simulating the influence of the Saleh nonlinearity.

Results and conclusions

For this attempt, the order of the Walsh-Hadamard sequence=5 and the number of subcarriers $N = 128$. The BER performance and comparison of the VSF-OFCDM system with PA modeled by the Saleh nonlinearity and ideal PA is shown in Figure 6.15d. It can be observed that from a BER=10^{-3} there is a difference between the distorted signal (marked with the 'Saleh' note in the legend) and the original non distorted signal of about 10dB to keep the same BER level. It should also be noted, that the BER performance can be improved by increasing the SF parameter. Increasing from SF=64 to SF=256 brings an improvement in SNR of about 5dB to preserve the BER performance.

This section describes the VSF-OFCDM system model and presents the results of analysis of the influence of the Saleh nonlinearity on signals generated by the above mentioned system and especially on BER performance of that system. It can be seen how the BER performances worsen when considering the Saleh nonlinearity; however, they can be improved by increasing the SF parameter. This is unfortunately redeemed with higher occupied frequency bandwidth. [6]

6.4.3 Out-of-band radiation and 2D spreading implementation using USRP

A small test site has been created in order to observe the real spectrum of the VSF-OFCDM system and the influence of the spreading factor, number of subcarriers and the PAPR minimizing algorithm introduced above. This test site is shown

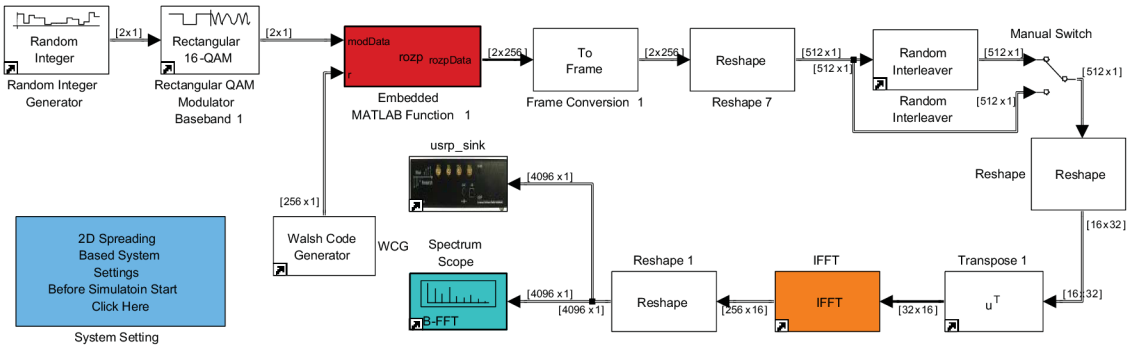

Fig. 6.17: An example of 16×16, $N = 32$ transmitter with upsampling factor 8. An interleaver is used.

in Figure 6.18.

The current subsection also shows a 2D spreading based system implementation using a Universal Radio Peripheral (USRP) [6, 7], [37] and results gained by measurement on this device. First of all, a short introduction of the USRP hardware is given as well as a description of its usage in the Simulink software.

The USRP hardware and The Simulink Blockset

The USRP contains a Field-Programmable Gate Array (FPGA) which can be reprogrammed, 4 high-speed Analog to Digital Converters (ADCs), 4 high-speed Digital to Analog Converters (DACs), and several auxiliary analog and digital IO and it can using a connected to a host computer by Universal Serial Bus (USB) 2.0 (480 Mb/s).

A blockset for Simulink was created at Karlsruhe Institute of Technology [38] to enable the possibility of effectively exploiting USRP. The blockset consists of three blocks. The *usrp_sink_block* is used to send data from Simulink to USRP and is solely studied in this subsection. The USRP is extended using the RFX2400 daughterboard with a frequency range 2.3 to 2.9 GHz and transmit power 50mW (17dBm).

The ROHDE&SCHWARZ SFQ3 signal analyzer is used for measuring of the spectra of received signals. A distance between the USRP transmitter and the ROHDE&SCHWARZ FSQ3 receiver d was set in the range from one to four decimeters but the influence of changing distance d was not observed.

An example of a 2D spreading based system implementation in Simulink is depicted in Figure 6.17.

The 2D spread signal used in this attempt can be represented with a matrix of data, shaped using the IFFT operation. The matrix construction using the Simulink

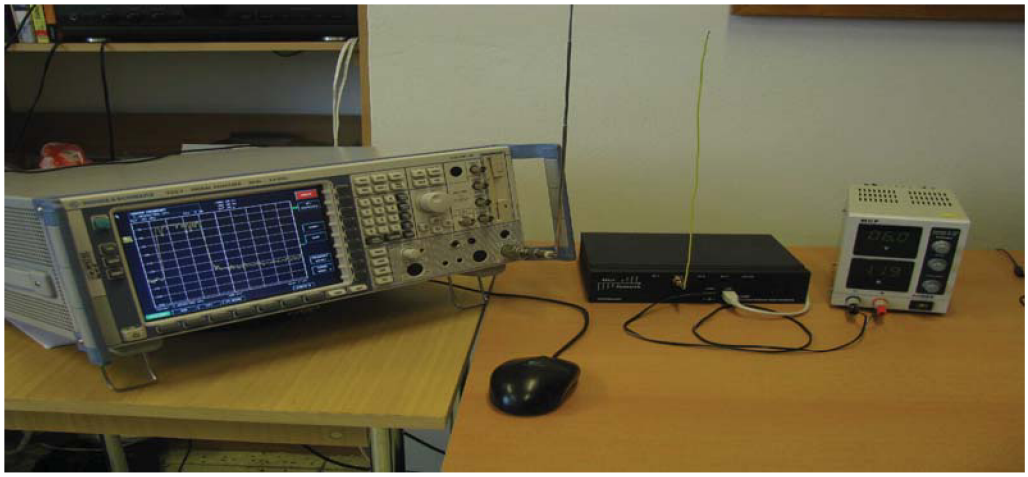

Fig. 6.18: The USRP work site, from left: The ROHDE&SCHWARZ SFQ3 signal analyzer, the USRP connected with PC (not depicted) using USB 2.0 and power supply (6V, DC)

blockset is apparent from figure 6.17. The IFFT block creates the orthogonality of the subcarriers according to the following equation:

$$s(t) = \sum_{n=-\infty}^{\infty} \sum_{m=0}^{M-1} a_n^m Rect_T(t - nT) e^{j2\pi m \frac{t}{T}}, \tag{6.20}$$

where m is the subcarrier number, n is the symbol order, a_n^m denotes the n-th symbol transmitted in the m-th subcarrier and finally $Rect_T$ is the rectangular window function with durability of T, which is defining for the OFDM symbol durability.

If the optional random interleaver is used, the values within the frame (the matrix) of one 16-QAM symbol in the direction of the axes x and y are not the same due to the random interleaving and in the direction of axis x due to the IFFT operation. The optional random chip interleaving block can be used for reducing of PAPR as was proposed in [33]. The principle of this method is as follows: the data stream of OFDM systems in the time domain can be considered as a sum of sinusoids and when the peak values of these sinusoids are optimally and mutually shifted, a sum of the peaks in one timeslot (and also PAPR) can be reduced.

It has been shown in [33] that the optimal interleaving pattern gives almost the same results as the random pattern which is used here and can be generated as a random permutation of the number of interleaved chips.

Results and conclusions

The results are shown in Figure 6.19. The marking of signals is as follows: $x_s(t)$ is the 2D spread time domain signal from Simulink, this is provided to USRP and its RFX2400 daughter-board for generation of the 2.4GHz $x_r(t)$ signal.

The interleaved releases of previously mentioned signals are supplemented with index $_i$ thus the marking of remaining signals is: $x_{s,i}(t)$ and $x_{r,i}(t)$.

In Figure 6.19, the spectral expressions of foregone signals $x_s(t)$, $x_r(t)$, $x_{s,i}(t)$ and $x_{r,i}(t)$ can be observed. It can be seen that the spectra of interleaved and non-interleaved signals $x_s(t)$ and $x_{s,i}(t)$ as well has the same bandwidth 250Hz, the received signals $x_r(t)$ and $x_{r,i}(t)$ were transmitted with carrier frequency 2.4GHz. The difference between signals $|X_s(f)|$ and $|X_{s,i}(f)|$ where $X(f) = FFT\{x(t)\}$ is expressed by the side lobs suppression feature.

The side lobs suppression is the main disadvantage of systems with interleaved chips. The non-interleaved system spectra reached suppression (in the band depicted in Figure 6.19) ca 150dB; however, the interleaved system reached only ca 40dB.

Nevertheless, the practical example consisting of the measured spectra shows that in the presence of noise, the side lobs suppression level 40dB is sufficient.

This chapter describes the results of implementation of the 2D spreading based system to the USRP. There is no fundamental divergence between the spectral expressions of interleaved and the non-interleaved systems except the side lobs suppression level; however, from a practical point of view this feature is negligible.

Bibliography of author's publications related to stated chapter:

[2] J. Blumenstein and Z. Fedra, "The PAPR and simple PAPR reduction of the 2D spreading based communication systems," *Radioengineering*, vol. 19, pp. 27 – 31, 2010.

[4] Z. Fedra and J. Blumenstein, "PAPR and amplitude distribution in MC-CDMA system," in *Computational Technologies in Electrical and Electronics Engineering (SIBIRCON), 2010 IEEE Region 8 International Conference* on, july 2010, pp. 247 –250.

[6] J. Blumenstein and Z. Fedra, "The 2d spreading based communication systems implementation using USRP," in *Radioelektronika (RADIOELEKTRONIKA), 2010 20th International Conference*, april 2010, pp. 1 –4.

[7] J. Blumenstein, "The impact of the saleh nonlinearity on the 2d spreading based system signals with high envelope fluctuations," in *ICECom, 2010 Conference Proceedings*, sept. 2010, pp. 1–4.

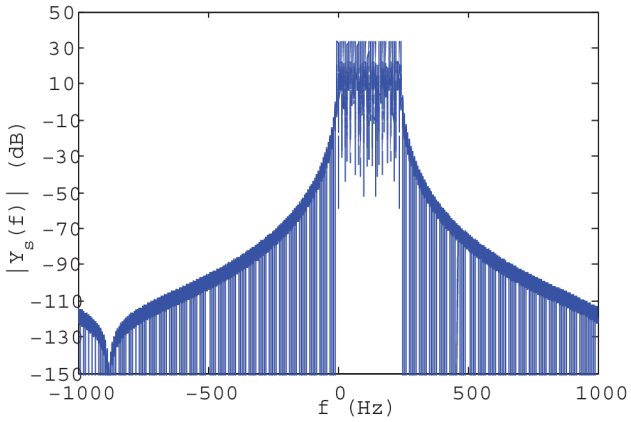

(a) $SF = 16 \times 16, N = 32$

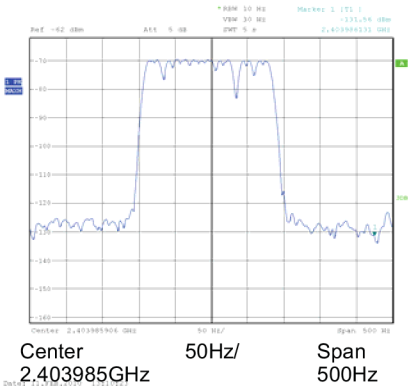

(b) $SF = 16 \times 16, N = 32$

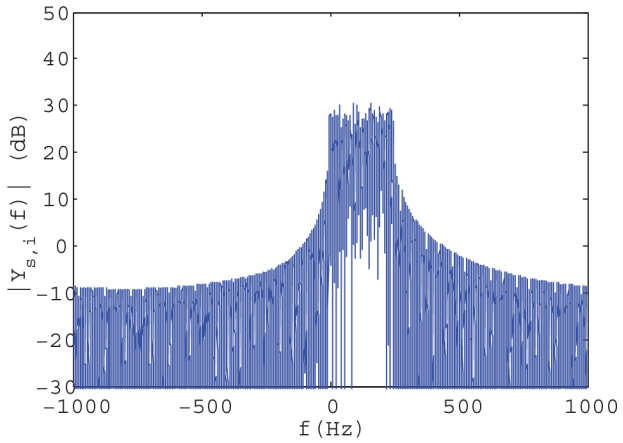

(c) $SF = 16 \times 16, N = 32$ interleaved

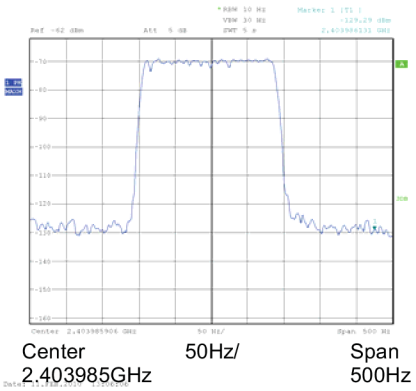

(d) $SF = 16 \times 16, N = 32$ interleaved

Fig. 6.19: The spectra of the transmitted signals $x_s(t)$, $x_r(t)$, $x_{s,i}(t)$ and $x_{r,i}(t)$.

Chapter 7

LTE link level simulations

This chapter gives a brief introduction of the LTE uplink link level simulator implementation and its structure. First of all, it needs to be stated that the downlink part of the LTE link level simulator has been introduced in [28], and the uplink implementation follows the same basic simulator structure and implementation concept as in the downlink. The simulator implementation structure is shown in Figure 7.1.

The simulation is performed in the main loop as shown in Figure 4.1: for given a CQI value/s and corresponding SNR vector, appropriate simulation parameters are loaded, which run the simulation for a configurable number of subframes (typically in the order of thousands to ensure appropriate BLER accuracy). The control channels are not implemented, their positions being filled with random data. The simulator currently implements an AWGN uplink channel, while the ACK/NACKs, which are calculated after decoding and transmitted back to the eNodeB, use an error-free genie feedback channel. Perfect channel knowledge is exploited so far; the reference symbols are filled with zeros. After processing all subframes of a given vector SNRs, the CQI value is shifted and the entire process with given SNRs runs again.

The simulator parameters can be configured in the `LTE_UL_sim_batch.m`, which batch-calls the simulator and contains the CQI and `LTE_UL_load_parameters.m`, which specifies simulator configuration parameters. There, the number of simulated subframes and SNR values can be configured, as well as parameters like the number of UEs and bandwidth. BER and throughput plots are shown after the simulation as figures of merit, enriched by confidence intervals.

Experiment and results

Current results of the proposed simulator are shown on 7.2a and 7.2b. The 99 % confidence intervals are plotted in order to provide a statistical perspective on the accuracy of the presented data.

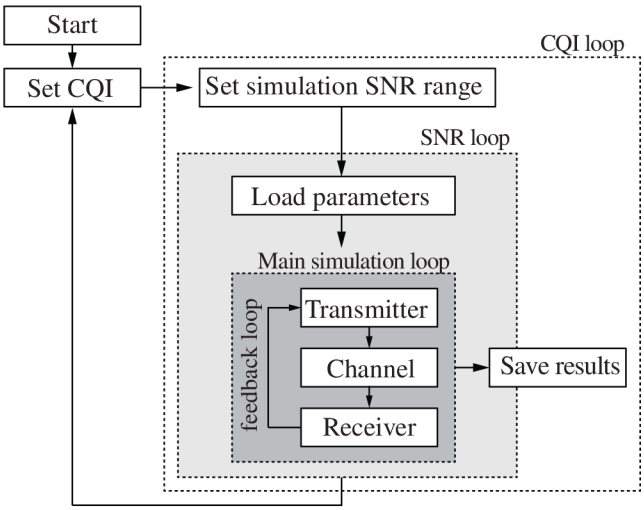

Fig. 7.1: Structure of the LTE uplink link level simulator.

7.2a and 7.2b show BER and throughput performance results of LTE uplink simulations for the 15 MCSs specified in 7.1. Compared to downlink results presented in [28], and after applying a correction factor for the fact that in uplink, three symbols are reserved for pilots, while downlink only uses two.

Compared to throughput results, 7.2b depicts the achievable system capacity as a theoretical upper bound. The achievable system capacity is given by Shannon's formula [39], adjusted to the particular system overheads in LTE uplink:

$$C = FB \log_2(1 + \mathrm{SNR}), \tag{7.1}$$

where B denotes the bandwidth of the simulated system, as in 7.3, SNR denotes the Signal to Noise Ratio, and F is a correction factor reflecting a reference losses due to Cyclic Prefix:

$$F = \frac{11}{14} \frac{T_{\mathrm{frame}} - T_{CP}}{T_{\mathrm{frame}}}. \tag{7.2}$$

The fraction $\frac{11}{14}$ gives the reference symbol losses. Out of the total of 14 OFDM symbols in the subframe, 11 are used for data, while 3 carry the Demodulation Reference Signals and Sounding Reference Signals.

The used system bandwidth B can thus be expressed as:

$$B = \frac{N_{\mathrm{sc}} N_{\mathrm{s}} N_{\mathrm{rb}}}{T_{\mathrm{sub}}}, \tag{7.3}$$

where N_{sc} is the number of subcarriers in one RB, N_{s} is the number of OFDM symbols in one subframe, and N_{rb} is the number of RBs.

Tab. 7.1: LTE system parameters of the presented uplink simulations

System Bandwidth	1.4 MHz
Subcarrier spacing	15 kHz
Subframe duration	1 ms
Number of UEs	1
Number of eNodeBs	1
Antenna Scheme	SISO
CP length	'normal' [10]
Channel	AWGN
Modulation	QPSK, ECR $= \left\{\frac{78}{1024}, \frac{120}{1024}, \frac{193}{1024}, \frac{308}{1024}, \frac{449}{1024}, \frac{602}{1024}\right\}$
and	16QAM, ECR $\in \{378, 490, 616\}$
Coding Schemes	64QAM, ECR $\in \{446, 567, 666, 772, 873, 938\}$

Conclusion

We presented LTE system and its major parameters and features in terms of physical layer. We also mentioned several differences between uplink and downlink parts. In addition, we show an open LTE link level simulator [8], implemented in MATLAB and available under a free academic non-commercial use license.

The uplink simulator is based on the structure of the open downlink simulator presented in [28]. The shown AWGN performance results confirm the ability of the simulator to work according to the 36' series 3GPP standards and enables easy reproducible research in the field of LTE uplink.

Bibliography of author's publications related to stated chapter:

[8] J. Blumenstein, J. C. Ikuno, J. Prokopec, and M. Rupp, "Simulating the long term evolution uplink physical layer," in *Proc. of the 53rd International Symposium ELMAR-2011*, Zadar, Croatia, 2011.

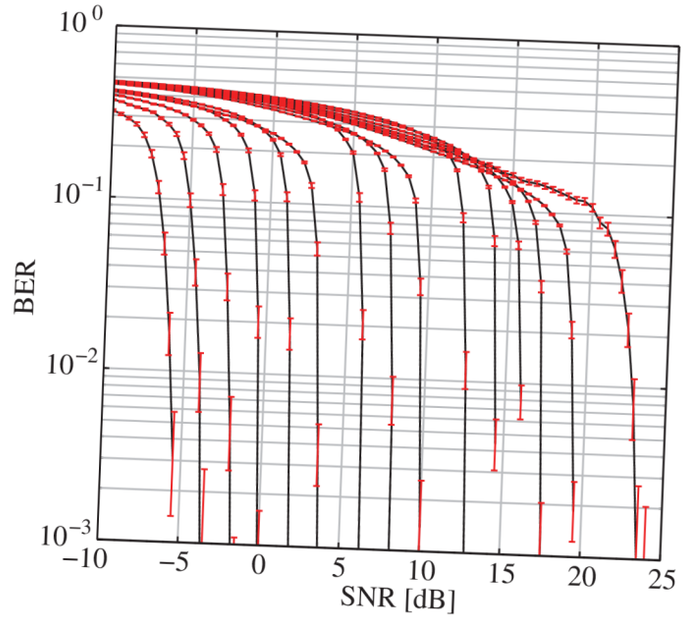

(a) Bit Error Ratio for different CQIs. Simulation parameters are shown in 7.1. The 99 % confidence intervals are depicted red.

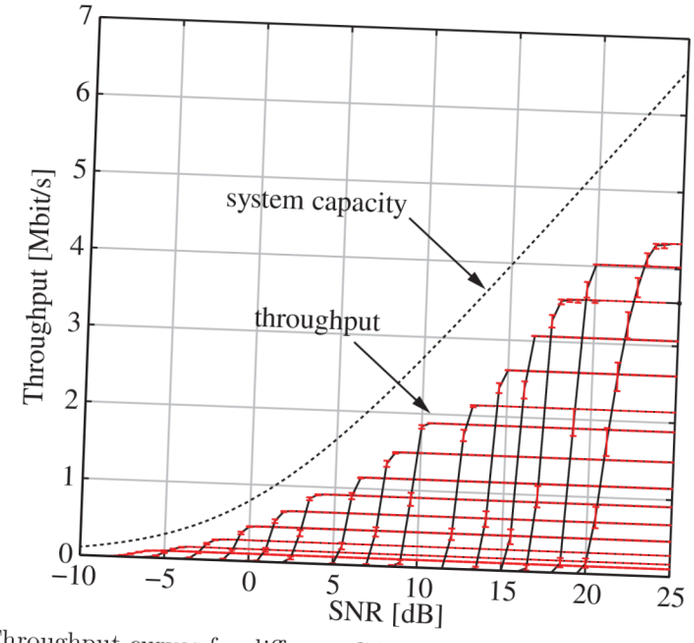

(b) Throughput curves for different CQIs with depicted confidence intervals and compared to system capacity (dotted line).

Fig. 7.2: An example of the LTE uplink simulator results.

7.1 Applicability of the 2D signal spreading in the UMTS LTE

7.1.1 Introduction

It is without any doubt that one of the main concerns of any communication system is to have the highest possible data throughput independent of the channel conditions. To maximize the throughput, we exploited time and frequency diversity. Apart from utilization of expensive techniques such as using extra bandwidth, adding more antennas or simply increasing the transmitting power, our method can be interpreted as a coding technique with code rate one. This method only increases the demand on computational power.

The idea behind this chapter is to reveal the efficiency of a 2D spreading method when it is incorporated in the most relevant wireless standard which is currently available. Therefore we chose an open source LTE simulator [19, 23, 28] to find out whether LTE can be enhanced by our proposed 2D signal spreading and show that it indeed outperforms a standard LTE downlink in terms of throughput.

An example of implementation of 2D signal spreading and thus a time-frequency diversity utilization can be found in VSF-OFCDM systems [3, 13, 31, 32]. The authors claim that the 2D spreading based VSF-OFCDM system exhibits a better performance than OFDM wireless transmission methods.

A three-cell frequency reuse OFDM system and one-cell reuse VSF-OFCDM system was compared. Due to the fact that VSF-OFCDM systems could benefit from the utilization of the code domain and the cells have been distinguished by a spreading code the VSF-OFCDM system reached significantly better throughput in a multi cell environment [40]. The reason for this is that the possibility to use the entire system bandwidth in the VSF-OFCDM system was enabled when compared to a third of the bandwidth in the case of pure OFDM.

LTE however uses a one-cell frequency reuse [20] and could benefit only from exploitation of the time-frequency diversity. To keep the comparison of 2D LTE and LTE fair, the bandwidth has to be the same as in the case of LTE.

When presenting our novel method, the need for comparing with a-state-the-art system is very important. Hence, the system model is based on the Vienna LTE simulator [19, 28] as a reference model. This simulator is released under a free non-commercial, academic use license. Such a release model enables algorithms to be tested and being compared using a common, known, and verifiable environment. We are certain that this transparency not only improves the quality of the published results but also their credibility.

Concerning results, we present throughput comparisons based on Power-Delay

Profile (PDP) channel models of the following types: Pedestrian channel model of type A (PedA), Pedestrian channel model of type B (PedB), Vehicular channel model of type A (VehA), Additive White Gaussian Noise (AWGN), Typical urban channel model (TU), ETU, Rural area channel model (RA) and Hilly terrain channel model (HT) [41, 42].

The remainder of this chapter is organized as follows: In the section System Model, the implementation of the 2D signal spreading into the LTE signal processing chain is described. In the section Spreading Factor we explain its selection and in the section Experiment and Results the comparison of the standard LTE downlink and the 2D spreading based LTE transmission is provided. At the end of the chapter, the section Conclusion rounds up the chapter.

The 2D spreading, as it is presented in [14], is rather repeating symbols which are multiplied by some spreading sequence. The resulting chips are repeated in time, frequency or code domain. The presented algorithm exploits one dimensional Walsh-Hadamard sequences. Nevertheless, due to interleaving of spread data among multiple carrier frequencies and multiple OFDM symbols, two dimensions are utilized. Therefore, we refer to this scheme as two-dimensional spreading.

Figure 7.3 represents the LTE signal processing chain. The dark gray blocks indicate additional blocks for 2D spreading and despreading. Other parts remain the same in both versions; 2D spreading based LTE and standard LTE downlink. The white blocks are according to 3GPP standards [10, 11, 12].

Vector $\mathbf{a_c}$ from Equation (7.4) denotes the CRC secured, segmented, scrambled, turbo-coded, rate matched, QAM and layer mapped data vector $\mathbf{a}$.

$$\mathbf{a_c} = (a_{\mathrm{c}1}, a_{\mathrm{c}2}, \ldots, a_{ce}) \,, \tag{7.4}$$

where the index e is the number of elements in the vector $\mathbf{a_c}$. We consider the output of the layer mapping block, vector $\mathbf{a_c}$, as the input of a 2D spreading block. In the 2D spreading block, vector $\mathbf{a_c}$ is chopped to SF parts, where SF stands for Spreading Factor - as explained below. This operation is illustrated by (7.5), where $\mathrm{SP}\{\mathbf{a_c}\}|_{\mathrm{SF}}$ denotes a Serial-to-parallel (SP) transformation of vector $\mathbf{a_c}$.

$$\mathrm{SP}\{\mathbf{a_c}\}|_{\mathrm{SF}} := \underbrace{\begin{pmatrix} a_{\mathrm{c}\,1} & a_{\mathrm{c}\,2} & \cdots & a_{\mathrm{c}\,\frac{e}{SF}} \\ a_{\mathrm{c}\left(\frac{e}{SF}+1\right)} & a_{\mathrm{c}\left(\frac{e}{SF}+2\right)} & \ddots & \vdots \\ \vdots & \ddots & a_{\mathrm{c}\,(e-SF-2)} & a_{\mathrm{c}\,(e-SF-1)} \\ a_{\mathrm{c}\,(e-SF)} & \cdots & \cdots & a_{ce} \end{pmatrix}}_{\mathbf{A_c}} . \tag{7.5}$$

Each row of matrix $\mathbf{A_c}$ is then multiplied by one Walsh-Hadamard sequence, i.e., one column of matrix $\boldsymbol{\Xi}$ specified by (7.7). This is described in Equation (7.6) and

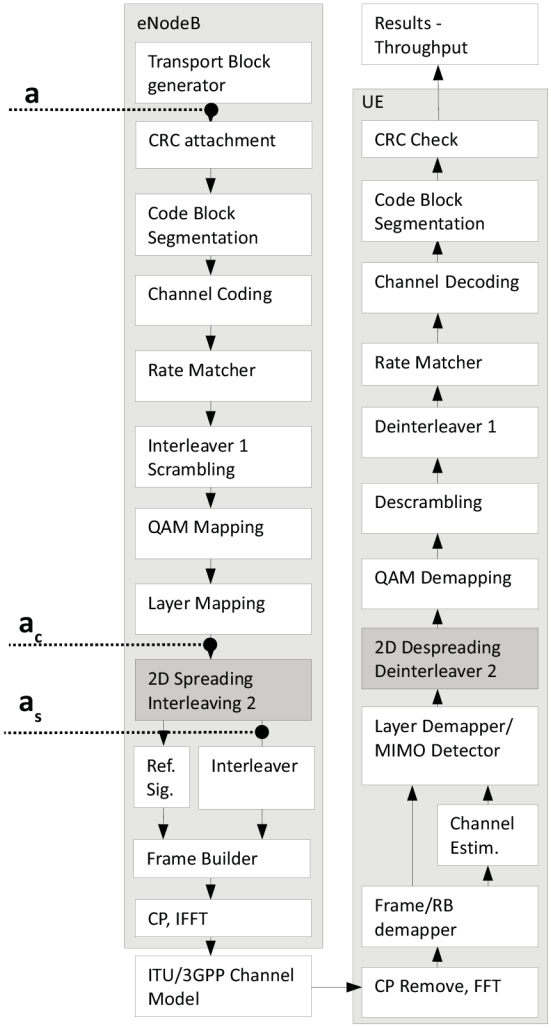

Fig. 7.3: The LTE signal processing chain. The dark gray blocks represents the additional blocks for 2D spreading and despreading. Other parts remain the same in both versions, 2D spreading based LTE and standard LTE. The white blocks are according to [10, 11, 12].

depicted in Figure 7.4.

$$\mathbf{A_s} = \mathbf{A_c}_{(i,*)} \otimes \mathbf{\Xi}_{(*,i)} =$$

$$= \begin{pmatrix} a_{\mathrm{c}\,1}\xi_{1,1} & a_{\mathrm{c}\left(\frac{e}{SF}+1\right)}\xi_{1,2} & \cdots & a_{\mathrm{c}\,(e-SF)}\xi_{1,SF} \\ a_{\mathrm{c}\,1}\xi_{2,1} & a_{\mathrm{c}\left(\frac{e}{SF}+1\right)}\xi_{2,2} & \vdots & \vdots \\ \vdots & \vdots & & \\ a_{\mathrm{c}\,1}\xi_{SF,1} & a_{\mathrm{c}\,2}\xi_{1,1} & \vdots & \vdots \\ a_{\mathrm{c}\,2}\xi_{1,1} & a_{\mathrm{c}\left(\frac{e}{SF}+2\right)}\xi_{1,2} & & \\ \vdots & \vdots & a_{\mathrm{c}\,(e-SF-2)}\xi_{SF-1,SF-1} & \vdots \\ a_{\mathrm{c}\,\frac{e}{SF}}\xi_{SF,1} & \vdots & a_{\mathrm{c}\,(e-SF-1)}\xi_{SF,SF-1} & a_{\mathrm{c}e}\xi_{SF,SF} \end{pmatrix}^T,$$

$$\forall i \in \{1, \ldots, SF\} \tag{7.6}$$

where

$$\mathbf{\Xi} = \begin{pmatrix} \xi_{1,1} & \cdots & \xi_{1,SF} \\ \vdots & & \vdots \\ \xi_{SF,1} & \cdots & \xi_{SF,SF} \end{pmatrix}. \tag{7.7}$$

Matrix $\mathbf{\Xi}$ then represents the Walsh-Hadamard matrix utilized as a bank of spreading sequences, $\mathbf{A_c}_{(i,*)}$ denotes the i-th row of matrix $\mathbf{A_c}$ and $\mathbf{\Xi}_{(*,i)}$ selects the i-th column of matrix $\mathbf{\Xi}$. The symbol $\otimes$ denotes the Kronecker product and $(.)^T$ denotes a matrix transposition.

Consequently, all the rows of the resulting matrix $\mathbf{A_s}$ are summed together according to Equation (7.8), thus we obtain a vector of spread data $\mathbf{a_s}$ of length SF. Each row of matrix $\mathbf{A_c}$ forms the code sheet, as shown in Figure 7.4.

$$\mathbf{a_s} = \sum_{j=1}^{SF} \mathbf{A_s}_{(j,*)} =$$

$$= \begin{bmatrix} a_{\mathrm{c}\,1}\xi_{1,1} + a_{\mathrm{c}\,1}\xi_{2,1} + & \cdots & +a_{\mathrm{c}\,\frac{e}{SF}}\xi_{SF,1} \\ a_{\mathrm{c}\left(\frac{e}{SF}+1\right)}\xi_{1,2} + a_{\mathrm{c}\left(\frac{e}{SF}+1\right)}\xi_{2,2} + & \cdots & +a_{\mathrm{c}\left(\frac{e}{SF}+1\right)}\xi_{SF,2} + a_{\mathrm{c}\left(\frac{e}{SF}+2\right)}\xi_{1,2} \\ & & \vdots \\ \vdots & \cdots & +a_{\mathrm{c}\,(e-SF-1)}\xi_{SF,SF-1} \\ a_{\mathrm{c}\,(e-SF)}\xi_{1,SF} + & \cdots & +a_{\mathrm{c}e}\xi_{SF,SF}. \end{bmatrix}^T \tag{7.8}$$

In order to spread the chips (the elements of vector $\mathbf{a_s}$) over the entire bandwidth and over all time slots (OFDM symbols), all positions of the chips are randomly interleaved.

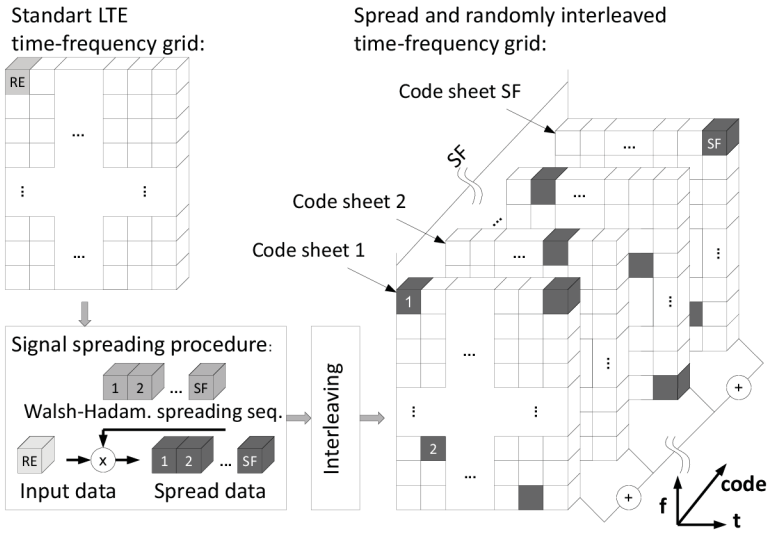

Fig. 7.4: The two-dimensional signal spreading process. We are spreading the signal right after the layer mapping block. The signal from the layer mapper is multiplied with all Walsh-Hadamard sequences of order SF. As a result we receive SF vectors, which represents the code-sheets. These are then summed together and we obtain a vector which serves as a frame builder input.

Vector $\mathbf{a_s}$, containing all the spread data is of the same length as the output of the layer mapping block, i.e., $\|\mathbf{a_s}\| = \|\mathbf{a_c}\|$.

Due to the fact that Walsh-Hadamard sequences are orthogonal, we are able to separate them at the receiver site. This principle is well-known from the CDMA systems [14].

When spreading a signal, we have SF-times more of data to transmit due to the spreading process, however, we also obtain SF times more space in the code domain which we can utilize. The increase in terms of data is in this case the same as the increase of the space dedicated to the transmission. As a result, after the summation of all the code sheets as presented in Figure 7.4, the amount of data is kept the same as in the case of standard LTE and thus no extra bandwidth is required.

However, the transmitted data occupies SF-times more time-frequency space, thus we gain on time-frequency diversity. At the receiver site, we have SF realizations of one bit. Due to the interleaving of these chips all over the transmission channel, the influence of deep fades of a transfer function [15] will be reduced.

The data share their space with other $\mathrm{SF} - 1$ data element. It will be shown in the next section that their performance on AWGN channels will not be improved.

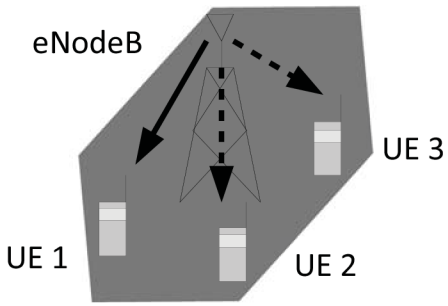

Fig. 7.5: For a lucidity of our experiment, we assume a perfect timing synchronization. If we consider that the whole available bandwidth is scheduled for a single user, here UE1, and omitting additional users (UE2 and UE3), we have simplified the transmission scheme. Thus we obtain a cell-specific throughput curve as seen in Figure 7.6.

7.1.2 Spreading Factor

For a better understanding of our proposed algorithm, a brief description of the LTE time-frequency signal grid according to [11] is stated in the following section. Using a 'normal' cyclic prefix, seven symbols with 12 subcarriers each form one resource block. One element of such a grid is called resource element (RE).

The maximal number of resource blocks transmitted in LTE is given by a total system bandwidth BW, where BW$\in \{1.4, 3, 5, 10, 15, 20\}$MHz. This corresponds to the number of resource blocks $N_{rb} \in \{6, 15, 25, 50, 75, 100\}$, which can be exploited for data transmission.

The spreading factor SF has to be chosen carefully, the length of the vector $\mathbf{a_c}$ representing the amount of transmitted data has to be divisible by SF. This is due to the fact that the 2D spreading block cuts its input vector $\mathbf{a_c}$ into SF parts in order to allow spreading. For a more detailed explanation, the chopped data are multiplied by the spreading sequence and then their length will be SF-times larger. The length of the spread data will then be exactly the same as the length of the 2D spreading block input vector $\mathbf{a_c}$. This is a necessary property. The frame builder can remain intact as well as the generation of pilot signals used for channel estimation. As a result, only minimal changes in the LTE standard are needed. Additionally, the comparison of such a system is more relevant.

In the configuration presented below, where BW=1.4MHz, the number of user equipments nUE=1, N_{rb}=6, a vector from the layer mapping block is of length 816 for the first subframe and 960 for the second subframe, respectively. Due to this, the maximal spreading factor is SF=48. The reason is that 48 is the highest common divider of 816 and 960 for which we also found a Walsh-Hadamard matrix.

Tab. 7.2: LTE system parameters of the novel 2D spreading based simulation scenario

System bandwidth	1.4 MHz
Subcarrier spacing	15 kHz
Subframe duration	1 ms
Number of UEs	1
Number of eNodeBs	1
Transmission Scheme	SISO
Number of subframes	10 000
CQI	15
SNR	30dB
SF	48
CP length	'normal' [10]
Channel estimation method	MMSE
Channel model	PedA, PedB, VehA, AWGN, TU, ETU, RA, HT [41, 42]

7.1.3 Experiment and results

This section describes the simulation setup as well as the results of the 2D spreading based LTE model.

Our method operates on the physical layer. Therefore, for a lucidity of our experiment, we assume a perfect time synchronization of all UEs which is provided by a higher layer. The resulting throughput curve, seen in Figure 7.6, is cell-specific and the scheduling of resource blocks is done by a scheduler which is also part of the higher layer of LTE functionality. If we consider that the whole available bandwidth is scheduled to one UE, we can simplify the transmission scheme as the single user environment as seen in Figure 7.5.

Regardless the Number of user equipments (nUE), but of course only when nUE> 1, our simulation setting generates maximal cell-specific data throughput given by the system bandwidth.

Figure 7.6 depicts the comparison of a standard compliant LTE downlink trans-

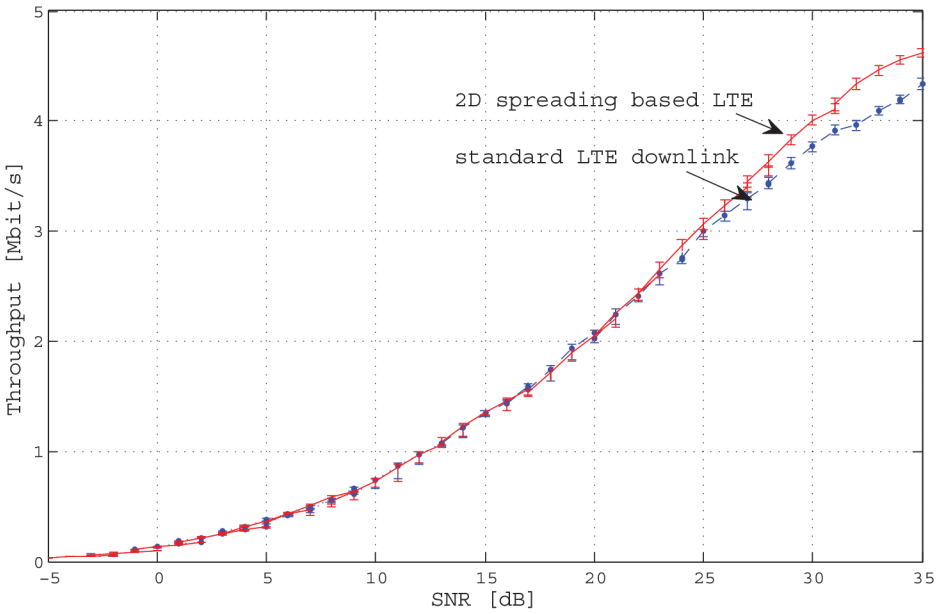

Fig. 7.6: The throughput curves for PedB channel model, 1.4MHz, single-user, 5000 sub-frames, CQIs from 1 to 15, SF=48 The 2D spreading based LTE is ploted in red, the standart LTE is dashed and blue. The 99% confidence intervals are also depicted, indicating a high confidence of the plotted results.

mission with a non standard compliant 2D LTE downlink. Adaptive CQI mapping's, for which the CQI is adapted in order to provide the highest possible data throughput at given SNR, are utilized. The setup of the simulation presented in Figure 7.6 is as follows: PedB channel model, 1.4MHz, single-user, 5000 subframes, CQIs from 1 to 15, SF=48. The 2D spreading based LTE transmission is plotted in red, the standard LTE transmission is dashed and blue. The 99% confidence intervals are also depicted in order to provide a statistical perspective on the accuracy of the presented data.

As can be observed, the 2D spreading enhanced LTE copes better in the multipath environment when compared to the standard LTE downlink. A considerable throughput improvement comes however only at rather high SNR around 25dB and more, depending on the channel model. A significant improvement is achieved at SNR=30dB according to Figure 7.6. In that case the 2D spreading enables a possibility to exploit higher CQI at a given SNR level in comparison with the standard form of LTE.

Table 7.2 gives an insight on important parameters of the next simulation, where we examined the 2D spreading influence applying a cornucopia of channel models, namely PedA, PedB, VehA, AWGN, TU, ETU, RA and HT [41, 42] which are available in the LTE simulator [19, 23]. Results are presented in Figure 7.7 where

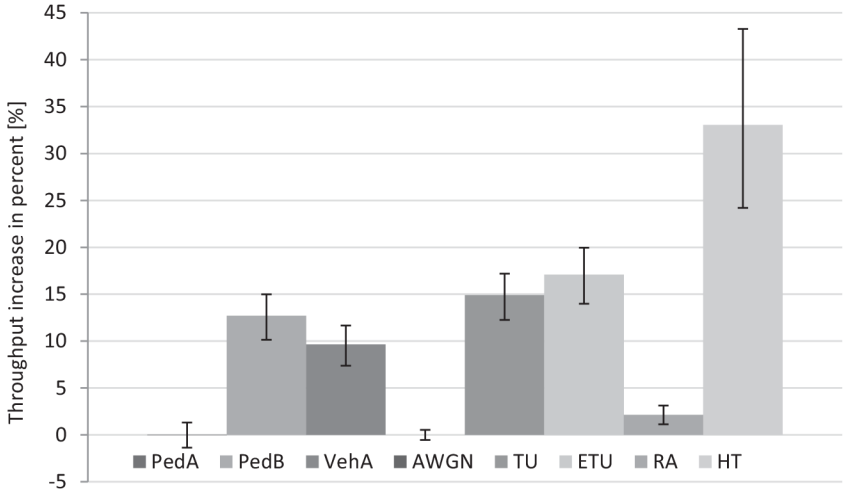

Fig. 7.7: The throughput increase for various channel models and for SNR=30dB. Simulation settings are listed in Table 7.2. The error bars represents 99% confidence intervals.

we can observe the throughput increase in percent. The 2D LTE achieves higher throughput and the increase is from 9% to more than 25% in five out of eight channel models. In one channel model the increase is about 2-3 percent. Only in 2 channel models, there is no increase at all.

Conclusion

This chapter describes a new 2D spreading mapping suitable for LTE transmissions. We implemented this algorithm into the state-of-the art simulation system developed at Vienna University of Technology. For a comparison of the proposed 2D spreading enhanced LTE and standard LTE downlink, several channel models have been applied.

The proposed spreading requires only minor modifications of LTE standards while brining considerable improvement in the throughput performance of such systems. We showed that in most channel models, the utilization of the 2D spreading is beneficial in terms of throughput increase. This increase ranges from 5 percent to more than 25 percent (99% confidence interval). It should also be noted, that the exploitation of the 2D spreading does not require extra bandwidth.

Chapter 8

Conclusion

This dissertation thesis is focused on the wireless communication systems based on Orthogonal Frequency Division Multiplexing (OFDM), Code Division Multiple Access (CDMA) systems and its combinations, specifically Variable Spreading Factor Orthogonal Frequency Code Division Multiplex (VSF-OFCDM).

A description of a wireless channel and its features as well as the description of the major ideas behind OFDM and CDMA is given in the state-of-the-art part. To provide a more specific insight on wireless communication systems, the Long Term Evolution (LTE) system has been chosen as the most current and promising system and, as such, a couple of the main ideas are also stated in the state-of-the-art part.

When summarized the main outcomes of this thesis are:

- We proposed a new channel estimation method based on code division. If we compare this code based method with the state-of-the-art pilot based method using the VSF-OFCDM simulator, we see that the new method benefits from notably lower Bit Error Ratio (BER). This is true for very low Doppler shifts. As the Doppler shift goes up, the code based method reaches the error floor faster than the pilot based method.
- An important finding is how Peak to Power Ratio (PAPR) grows with growing SF_t, but not with SF_f . This feature can be profitably used in designing various SF patterns in VSF-OFCDM systems. Last but not least we have shown that PAPR can be simply and effectively reduced nearly to the OFDM PAPR.
- We made the analysis of the VSF-OFCDM system model exploiting the Saleh nonlinearity. It can be seen how the BER performances worsen when considering Saleh nonlinearity and how they can be improved by increasing the Spreading factor (SF) parameter. This is unfortunately redeemed with higher occupied frequency bandwidth.

- We revealed that the new method of 2D signal spreading brings considerable improvement in the throughput performance of LTE downlink. We showed that in most channel models, the utilization of 2D spreading is beneficial in terms of throughput increase. This increase ranges from 5 percent to more than 25 percent (99% confidence interval). It should also be noted, that the exploitation of 2D spreading does not require extra bandwidth.

Author's publications

[1] J. Blumenstein and Z. Fedra, "The characteristics of the 2D spreading based communication systems," in *Radioelektronika, 2009. RADIOELEKTRONIKA '09. 19th International Conference*, april 2009, pp. 279 –281.

[2] ——, "The PAPR and simple PAPR reduction of the 2D spreading based communication systems," *Radioengineering*, vol. 19, pp. 27 – 31, 2010.

[3] J. Blumenstein, Z. Fedra, and V. Šebesta, "Performance of pilot aided channel estimation technique in 2D spreading based systems," *Radioengineering*, vol. 19, pp. 507–510, 2010.

[4] Z. Fedra and J. Blumenstein, "PAPR and amplitude distribution in MC-CDMA system," in *Computational Technologies in Electrical and Electronics Engineering (SIBIRCON), 2010 IEEE Region 8 International Conference on*, july 2010, pp. 247 –250.

[5] [Online]. Available: http://www.urel.feec.vutbr.cz/~fedra/

[6] J. Blumenstein and Z. Fedra, "The 2D spreading based communication systems implementation using USRP," in *Radioelektronika (RADIOELEKTRONIKA), 2010 20th International Conference*, april 2010, pp. 1 –4.

[7] J. Blumenstein, "The impact of the Saleh nonlinearity on the 2D spreading based system signals with high envelope fluctuations," in *ICECom, 2010 Conference Proceedings*, sept. 2010, pp. 1 –4.

[8] J. Blumenstein, J. C. Ikuno, J. Prokopec, and M. Rupp, "Simulating the Long Term Evolution Uplink Physical Layer," in *Proc. of the 53rd International Symposium ELMAR-2011*, Zadar, Croatia, 2011.

[9] J. Blumenstein, J. Poměnková, and R. Mašálek, "Comparative study of time- frequency analysis approaches with application to economic indicators." in *26th European Conference on Modeling and Simulation ECMS 2012*, Koblenz, Germany, 2012.

Other sources

[10] 3GPP Technical Specification Group RAN, "E-UTRA; physical channels and modulation," 3GPP, Tech. Rep. TS 36.211 Version 8.7.0, May 2009.

[11] ——, "E-UTRA; multiplexing and channel coding," 3GPP, Tech. Rep. TS 36.212, March 2009.

[12] ——, "E-UTRA; physical layer procedures," 3GPP, Tech. Rep. TS 36.213, March 2009.

[13] N. Maeda, Y. Kishiyama, H. Atarashi, and M. Sawahashi, "Variable spreading factor-ofcdm with two dimensional spreading that prioritizes time domain spreading for forward link broadband wireless access," in *Vehicular Technology Conference, 2003. VTC 2003-Spring. The 57th IEEE Semiannual*, vol. 1, april 2003, pp. 127 – 132 vol.1.

[14] K. Fazel and S. Kaiser, *Multi-carrier and spread spectrum systems: from OFDM and MC-CDMA to LTE and WiMAX*. Wiley, 2008. [Online]. Available: http://books.google.com/books?id=RzUJsPqe-dgC

[15] L. Hanzo, *OFDM and MC-CDMA for broadband multi-user communications, WLANs, and broadcasting*. J. Wiley, 2003. [Online]. Available: http://books.google.com/books?id=hQ6bl3RG04sC

[16] K. Zheng, G. Zeng, and W. Wang, "Performance analysis for OFDM-CDMA with joint frequency-time spreading," *Broadcasting, IEEE Transactions on*, vol. 51, no. 1, pp. 144 – 148, march 2005.

[17] S. Sesia, M. Baker, and I. Toufik, *LTE, the UMTS long term evolution: from theory to practice*. Wiley, 2009. [Online]. Available: http://books.google.com/books?id=E2ppetS3D7cC

[18] J. Ikuno, M. Wrulich, and M. Rupp, "System level simulation of LTE networks," in *Vehicular Technology Conference (VTC 2010-Spring), 2010 IEEE 71st*, may 2010, pp. 1 –5.

[19] [Online]. Available: http://www.nt.tuwien.ac.at/ltesimulator/

[20] S. Sesia, I. Toufik, and M. Baker, *LTE, The UMTS Long Term Evolution: From Theory to Practice*. John Wiley & Sons, 2009.

[21] R. Marsalek, "On the reduced complexity interleaving method for OFDM PAPR reduction," *Radioengineering*, vol. 15, no. 3, Sep. 2006. [Online]. Available: http://www.radioeng.cz/fulltexts/2006/06_03_49_53.pdf

[22] J. Tellado, *Multicarrier modulation with low par: applications to DSL and wireless*, ser. Kluwer international series in engineering and computer science. Kluwer Academic Publishers, 2000. [Online]. Available: http://books.google.cz/books?id=QlUmgxcckCYC

[23] C. Mehlführer, J. Colom Ikuno, M. Simko, S. Schwarz, M. Wrulich, and M. Rupp, "The vienna LTE simulators - enabling reproducibility in wireless communications research," *EURASIP Journal on Advances in Signal Processing*, vol. 2011, no. 1, p. 29, 2011. [Online]. Available: http://asp.eurasipjournals.com/content/2011/1/29

[24] M. Šimko, C. Mehlführer, T. Zemen, and M. Rupp, "Inter-Carrier Interference Estimation in MIMO OFDM Systems with Arbitrary Pilot Structure," in *Proc. IEEE VTC Spring 2011*, Hungary, May 2011.

[25] Q. Wang, C. Mehlführer, and M. Rupp, "Carrier frequency synchronization in the downlink of 3GPP LTE," in *Proceeding of the 21st Annual IEEE International Symposium on Personal, Indoor and Mobile Radio Communications (PIMRC'10)*, Istanbul, Turkey, Sep. 2010.

[26] J. C. Ikuno, C. Mehlfürer, and M.Rupp, "A novel LEP model for OFDM systems with HARQ," in *Proc. IEEE International Conference on Communications (ICC) 2011*, June 2011.

[27] S. Schwarz, M. Wrulich, and M. Rupp, "Mutual information based calculation of the precoding matrix indicator for 3GPP UMTS/LTE," in *ITG International Workshop on Smart Antennas (WSA)*, Bremen, Germany, February 2010.

[28] C. Mehlführer, M. Wrulich, J. C. Ikuno, D. Bosanska, and M. Rupp, "Simulating the Long Term Evolution physical layer," in *European Signal Processing Conference (EUSIPCO)*, Glasgow, Scotland, August 2009.

[29] B. E. Priyanto, H. Codina, S. Rene, T. B. Sorensen, and P. Mogensen, "Initial Performance Evaluation of DFT-Spread OFDM Based SC-FDMA for UTRA LTE Uplink," in *Vehicular Technology Conference, 2007. VTC2007-Spring. IEEE 65th*, 2007.

[30] P. Frenger, S. Parkvall, and E. Dahlman, "Performance comparison of HARQ with chase combining and incremental redundancy for HSDPA," *Proc. VTS IEEE 54th Vehicular Technology Conference Fall VTC*, 6001.

[31] H. Atarashi, N. Maeda, S. Abeta, and M. Sawahashi, "Broadband packet wireless access based on VSF-OFCDM and MC/DS-CDMA," in *Personal, Indoor and Mobile Radio Communications, 2002. The 13th IEEE International Symposium on*, vol. 3, sept. 2002, pp. 992 – 997 vol.3.

[32] N. Maeda, H. Atarashi, S. Abeta, and M. Sawahashi, "Throughput comparison between VSF-OFCDM and OFDM considering effect of sectorization in forward link broadband packet wireless access," in *Vehicular Technology Conference, 2002. Proceedings. VTC 2002-Fall. 2002 IEEE 56th*, vol. 1, 2002, pp. 47 – 51 vol.1.

[33] Z. Fedra and V. Sebesta, "The new PAPR reduction approach in MC-CDMA," in *Signal Processing Symposium, 2006. NORSIG 2006. Proceedings of the 7th Nordic*, june 2006, pp. 270 –273.

[34] P. Hoeher, S. Kaiser, and P. Robertson, "Two-dimensional pilot-symbol-aided channel estimation by wiener filtering," in *Acoustics, Speech, and Signal Processing, 1997. ICASSP-97., 1997 IEEE International Conference on*, vol. 3, apr 1997, pp. 1845 –1848 vol.3.

[35] A. Saleh, "Frequency-independent and frequency-dependent nonlinear models of twt amplifiers," *Communications, IEEE Transactions on*, vol. 29, no. 11, pp. 1715 – 1720, nov 1981.

[36] [Online]. Available: http://www.mathworks.com/help/toolbox/rfblks/amplifier.html

[37] [Online]. Available: http://www.ettus.com/

[38] [Online]. Available: http://www.cel.kit.edu/usrp.php.

[39] C. E. Shannon, "A mathematical theory of communication," *Bell Systems Technical Journal*, vol. 27, pp. 379–423,623–656, 1948.

[40] C.-C. Chong, F. Watanabe, H. Inamura, D. Wang, H. Minn, and N. Al-Dhahir, "On the performance comparison of vsf-ofcdma and ofdma," in *Personal, Indoor and Mobile Radio Communications, 2008. PIMRC 2008. IEEE 19th International Symposium on*, sept. 2008, pp. 1 –6.

[41] "Recommendation itu-r m.1225: Guidelines for evaluation of radio transmission technologies for imt-2000," Tech. Rep., Tech. Rep., 1997.

[42] 3GPP, "Technical specification group radio access network; deployment aspects (release 7)," 3GPP, Tech. Rep. 25.943 V7.0.0, Jan 2007.

[43] H. Harada and R. Prasad, *Simulation and software radio for mobile communications*, ser. The Artech House universal personal communications series. Artech House, 2002, no. sv. 1. [Online]. Available: http://books.google.com/books?id=amhNM01OKCUC

[44] 3GPP Technical Specification Group RAN, "E-UTRA; LTE physical layer – general description," 3GPP, Tech. Rep. TS 36.201 Version 8.3.0, March 2009.

[45] E. Dahlman, S. Parkvall, J. Skold, and P. Beming, *3G Evolution: HSDPA and LTE for Mobile Broadband*. Academic Press, July 2007.

[46] P. Vandewalle, J. Kovacevic, and M. Vetterli, "Reproducible research in signal processing," *Signal Processing Magazine, IEEE*, vol. 26, no. 3, pp. 37 –47, may 2009.

List of Acronyms

3GPP 3rd Generation Partnership Project
ADC Analog to Digital Converter
ADSL Asymmetric Digital Subscriber Line
AWGN Additive White Gaussian Noise
BER Bit Error Ratio
BPSK Binary Phase Shift Keying
BLER Block Error Ratio
CP Cyclic Prefix
CB Code Block
CCDF Complementary Cumulative Distribution Function
CDMA Code Division Multiple Access
CRC Cyclic Redundancy Check
CQI Channel Quality Indicator
CSI Channel State Information
DFT Discrete Fourier Transform
DAC Digital to Analog Converter
DVB-T Digital Video Broadcasting – Terrestrial
ECR Effective Code Rate
ETU Extended typical urban channel model
EVA Extended vehicular channel model
EPA Extended pedestrian channel model
FDMA Frequency Division Multiple Access
FFT Fast Fourier Transform
FPGA Field-Programmable Gate Array
GPS Global Positioning System
HARQ Hybrid Automatic Repeat Request
HT Hilly terrain channel model
IFFT Inverse Fast Fourier Transform
ICI Inter Carrier Interference
ISI Inter Symbolic Interference
ITU International Telecommunication Union
LTE Long Term Evolution
MC-CDMA Multi-Carrier Code Division Multiple Access
MCS Modulation and Coding Schemet
nUE Number of user equipments
OFDM Orthogonal Frequency Division Multiplexing
OFDMA Orthogonal Frequency Division Multiple Access

OOB Out-of-Band
PA Power Amplifier
PAPR Peak to Power Ratio
PC Personal Computer
PDA Personal Digital Assistant
PDP Power-Delay Profile
PedA Pedestrian channel model of type A
PedB Pedestrian channel model of type B
PSK Phase Shift Keying
PS Parallel Serial
PST Parallel Serial Transmitter
RA Rural area channel model
RB Resource Block
RE Resource Element
SC-FDMA Single-carrier FDMA
SF Spreading factor
SP Serial to Parallel
SNR Signal to Noise Ratio
QAM Quadrature Amplitude Modulation
QPSK Quadrature Phase Shift Keying
TB Transport Block
TDMA Time Division Multiple Access
TB Transport Block
TU Typical urban channel model
UE User Equipment
UL-SCH Uplink Shared Channel
UMTS Universal Mobile Telecommunications System
USB Universal Serial Bus
USRP Universal Radio Peripheral
VehA Vehicular channel model of type A
VSF-OFCDM Variable Spreading Factor Orthogonal Frequency Code Division Multiplex
WCDMA Wideband CDMA
WSS-US Wide-Sense Stationary Uncorrelated Scattering

List of Symbols

$\odot$ - Hadamard product

$\otimes$ - Kronecker product

$(.)^T$ - matrix transposition

$\mathbf{a}^{x,u}$ - x-th VSF-OFCDM symbol of the u-th user

$\mathbf{a}_{\mathrm{s}}^{x,u}$ - x-th spread VSF-OFCDM symbol of the u-th user

$\mathbf{a_c}$ - an input vector of 2D spreading block in 2D LTE system

$\mathbf{a_s}$ - a vector of 2D LTE spread data

$a_k^{x,u}$ - k-th elemDent of the vector $\mathbf{a}^{x,u}$

$\mathbf{a}_{\mathrm{r\,PSR}}^{x,u}$ - signal $\mathbf{a}_{\mathrm{r}}^{x,u}$ transformed according formula 6.12

$\mathbf{a}_{\mathrm{r}}$ - FFT of the received signal

$\mathbf{a}_{\mathrm{C}}^{x,u}$ - VSF-OFCDM symbol which is corrected by vector ζ^x containing the CSI

$\boldsymbol{A_c}$ - SF_{LTE} transformed vector $\mathbf{a_c}$

$\boldsymbol{A_s}$ - matrix of spread data in 2D LTE system

$\boldsymbol{A}_{\boldsymbol{c}(i,*)}$ - the i-th row of matrix $\boldsymbol{A_c}$

e - number of elements in the vector $\mathbf{a_c}$

EG_f - estimation grid in frequency domain

EG_t - estimation grid in time domain

f_{Dr} - Doppler shift

ΔF - spacing of the subcarriers

f_S - expresses the Saleh nonlinearity

$_{k,n}$ - row and column index in the matrix $\mathbf{s}_{\mathrm{PST}}^{u,x}$

N - number of subcarriers

$\mathbf{r}$ - received signal

$\mathbf{s}_m^{u,x}$ - VSF-OFCDM frame

$\mathbf{s}_m^{u,x}$ - column of the $\mathbf{s}_m^{u,x}$ matrix

$\mathbf{s}_{\mathrm{PST}}^{u,x}$ - from paralel to serial transformed signal $\mathbf{s}_m^{u,x}$

SF - spreading factor

SF_t - spreading factor in the time domain

SF_f - spreading factor the in frequency domain

T - time duration of one VSF-OFCDM frame

t_s - sample time

u - user order

U - total number of code channels

x - time index

ξ^u - Hadamard spreading sequence of the u-th user

ξ^u_{SF} - SF-th element of the vector ξ^u

$\mathbf{\Xi}$ - Walsh-Hadamard matrix utilized as a bank of spreading sequences in the 2D LTE system

$\mathbf{\Xi}_{(*,i)}$ - the i-th column of matrix $\mathbf{\Xi}$

$\boldsymbol{\xi}^u$ - matrix of spreading sequences ξ^u

$\eta(t)$ - additive white Gaussian noise

$\boldsymbol{\zeta}$ - a channel state information (CSI) vector